The Astrophysical Journal, 805:72 (25pp), 2015 May 20 doi:10.1088/0004-637X/805/1/72

ABUNDANT CH_3OH MASERS BUT NO NEW EVIDENCE FOR STAR FORMATION IN GCM0.253+0.016

E. A. C. Mills[1,5,6], N. Butterfield[2], D. A. Ludovici[2], C. C. Lang[2,3], J. Ott[1,6], M. R. Morris[4], and S. Schmitz[2]
[1] National Radio Astronomy Observatory, 1003 Lopezville Rd, Socorro, NM 87801, USA; bmills@aoc.nrao.edu
[2] Department of Physics and Astronomy, University of Iowa, Iowa City, IA 52245, USA
[3] School of Mathematics and Physics, University of Tasmania Private Bag 37, Hobart, Tasmania 7001, Australia
[4] Department of Physics and Astronomy, University of California, 430 Portola Plaza, Box 951547 Los Angeles, CA 90095-1547, USA
Received 2015 February 11; accepted 2015 March 23; published 2015 May 21

ABSTRACT

We present new observations of the quiescent giant molecular cloud GCM0.253+0.016 in the Galactic center, using the upgraded Karl G. Jansky Very Large Array. Observations were made at wavelengths near 1 cm, at the K (24–26 GHz) and Ka (27 and 36 GHz) bands, with velocity resolutions of 1–3 km s^{-1} and spatial resolutions of ~0.1 pc, at the assumed 8.4 kpc distance of this cloud. The continuum observations of this cloud are the most sensitive yet made, and reveal previously undetected emission which we attribute primarily to free–free emission from external ionization of the cloud. In addition to the sensitive continuum map, we produce maps of 12 molecular lines: 8 transitions of NH_3–(1, 1), (2, 2), (3, 3), (4, 4), (5, 5), (6, 6), (7, 7), and (9, 9), as well as the HC_3N (3–2) and (4–3) lines, and CH_3OH 4_{-1}–3_0, the latter of which is known to be a collisionally excited maser. We identify 148 CH_3OH 4_{-1}–3_0 (36.2 GHz) sources, of which 68 have brightness temperatures in excess of the highest temperature measured for this cloud (400 K) and can be confirmed to be masers. The majority of these masers are concentrated in the southernmost part of the cloud. We find that neither these masers nor the continuum emission in this cloud provide strong evidence for ongoing star formation in excess of that previously inferred by the presence of an H_2O maser.

Key words: Galaxy: center

1. INTRODUCTION

Molecular gas in the central 500 parsec of the Galaxy (the Central Molecular Zone or CMZ) is concentrated in a population of giant molecular clouds with sizes of 15–50 pc, and masses of 10^4–10^6 $M_\odot$ (e.g., Molinari et al. 2011). On scales of a few parsecs, these CMZ clouds are characterized by large, turbulent linewidths (15–50 km s^{-1}, Bally et al. 1987), high gas temperatures (50–300 K, Mauersberger et al. 1986; Hüttemeister et al. 1993), and substantial densities ($n > 10^4$ cm^{-3}, Zylka et al. 1992). However, apart from the Sgr B2 cloud (in which there are dozens of compact and hypercompact H II regions as well as two massive hot cores and numerous water masers, indicating an extremely active star-forming environment, Cheung et al. 1969; Vogel et al. 1987; Gaume & Claussen 1990; de Pree et al. 1998), most CMZ clouds show little evidence of recent or ongoing star formation (Guesten & Downes 1983; Ho et al. 1985; Morris 1989, 1993; Lis et al. 1994; Caswell 1996; Immer et al. 2012).

Exactly why CMZ clouds exhibit so little ongoing star formation is unclear. Given that the total amount of molecular gas in this region (~3×10^7 $M_\odot$, Dahmen et al. 1998) is just under 5% of the total molecular gas in the Galaxy (~8.4×10^8 $M_\odot$; Nakanishi & Sofue 2006), and the star formation rate in the CMZ makes up a similar fraction of the total estimated star formation rate in the Galaxy (Longmore et al. 2013), there would not immediately appear to be a discrepancy. The difference is that gas in the CMZ is believed to be on average two orders of magnitude more dense than elsewhere in the Galaxy and might thus be expected to be forming stars at a proportionately higher rate (Lada et al. 2012; Longmore et al. 2013). If the CMZ deviates from relations between the amount of dense ($n > 10^4$ cm^{-3}) gas and star formation which hold in other galaxies, this could suggest that star formation might proceed differently in such extreme environments (e.g., Kruijssen et al. 2014). Or, it may indicate that the ongoing star formation in CMZ clouds is underestimated using traditional indicators. It has also been suggested that we may be observing many CMZ clouds at a special time, just before the (possibly triggered) onset of star formation (Longmore et al. 2013; Kruijssen et al. 2015). A final consideration is that, especially in regions with short orbital timescales like the CMZ, one must be careful to compare the amount of gas and star formation on spatial scales sufficiently large (and timescales sufficiently long) for them to be correlated (Kruijssen & Longmore 2014). Ultimately, whether or not the star formation process in the CMZ is truly unusual, observing CMZ clouds lacking in star formation is a unique opportunity to investigate the initial conditions of (massive) star formation in an extreme environment, before the star formation process itself begins to affect and further disrupt that environment.

1.1. GCM0.253+0.016

GCM0.253+0.016 (also, G0.253+0.016, G0.216+0.016, M0.25+0.01, M0.25+0.11, or "The Brick," as it has been variously referred to in the literature) is one such extremely quiescent CMZ cloud, located ~45 pc in projection from the dynamical center of the Galaxy (assuming a Galactocentric distance of 8.4 kpc; Ghez et al. 2008; Gillessen et al. 2009; Reid et al. 2014). Although its appearance as a prominent infrared dark cloud indicates that it is occulting most of the infrared emission from the nuclear bulge; its chemistry, kinematics, high temperatures, and large linewidths are all

[5] E.A.C. Mills is a Jansky Fellow of the National Radio Astronomy Observatory.
[6] The National Radio Astronomy Observatory is a facility of the National Science Foundation operated under cooperative agreement by Associated Universities, Inc.

consistent with being located at the CMZ, and it is commonly taken to lie on the near side of the CMZ (Lis & Menten 1998). In total, GCM0.253+0.016 is suggested to have a mass of 1–2 × 10^5 $M_\odot$, making it one of the five most massive clouds in the CMZ (Lis et al. 1994; Longmore et al. 2012). It is also the only compact >10^4 solar mass cloud found thus far in the entire Galaxy which does not exhibit advanced stages of star formation (Ginsburg et al. 2012; Tackenberg et al. 2012; Urquhart et al. 2014). The comparably massive Maddalena cloud in the outer Galaxy, which also does not show evidence of active massive star formation, is extended over ∼100 pc. (Maddalena & Thaddeus 1985; Megeath et al. 2009). The large mass and relatively high average density of this cloud ($n \sim 1 \times 10^5$ cm^{-3}; Longmore et al. 2012; Kauffmann et al. 2013) suggest that it is capable of massive star and perhaps even cluster formation (Longmore et al. 2012). However, there is no clear evidence in this cloud for ongoing massive star formation apart from a single water maser (Lis et al. 1994).

Recent continuum studies of GCM0.253+0.016 at infrared to radio wavelengths have continued to search for signposts of ongoing star formation. Longmore et al. (2012) analyze Herschel observations of the cloud and find no embedded heating sources at wavelengths up to 70 μm. At 280 GHz with the SMA, Kauffmann et al. (2013) find only one strong, compact dust core, which they suggest is indicative of a low potential for star formation (but see also Johnston et al. 2014, who find more extensive dust continuum emission at 230 GHz, also with the SMA). Both Johnston et al. (2014) and Rathborne et al. (2014b) then measure the column density probability distribution function (PDF) from the dust continuum, finding it to be log-normal. Rathborne et al. (2014b) do find a deviation from this form at high column densities (interpreted as self-gravitation), but state that this corresponds to just the single dust core already known to contain a water maser. The only potential indications of more advanced star formation come from high-resolution radio observations by Rodríguez & Zapata (2013) who identify three compact thermal continuum sources which they suggest could be embedded B-stars. However, all of these sources are located outside of the bulk of the gas and dust emission in the cloud, on its periphery.

Although continuum observations show few signs of previously missed star formation and are largely consistent with GCM0.253+0.016 being in a quiescent, pre-star-forming stage, a host of recent observations of the gas reveal many other complexities. Velocity dispersions on spatial scales of 0.07–0.1 pc are observed to range from extremely turbulent (>30 km s^{-1} as measured in ALMA observations of SO; Higuchi et al. 2014) to clumps with line widths apparently less than 1 km s^{-1} (from SMA observations of the quiescent gas tracer N_2H^+, Kauffmann et al. 2013)—the narrowest line widths yet observed in a CMZ cloud. Abundant emission from other shock-tracing molecules SiO and CH_3OH are additionally observed in GCM0.253+0.016 by Rathborne et al. (2015) and Johnston et al. (2014). Johnston et al. (2014) also present the first resolved temperature measurements of the cloud, using H_2CO, which indicate extremely high temperatures in the clumpy gas ($T \sim 300$ K), much higher than temperatures measured from single-dish observations of the same lines (Ao et al. 2013), though comparable to temperatures measured in this cloud from single-dish observations of highly excited lines of NH_3 (Mills & Morris 2013). The most surprising new observations are of a series of HCO^+ absorption filaments, suggested to be tracing the surface magnetic field lines in the cloud, which which have never before been seen in any giant molecular cloud (Bally et al. 2014).

Complementing this existing suite of molecular line observations, we present the first interferometric study of both the molecular and ionized gas in GCM0.253+0.016 at radio wavelengths, using the Karl G. Jansky Very Large Array (hereafter, "VLA"), a facility of the National Radio Astronomy Observatory.[7] The upgraded VLA offers more sensitive receivers and broad spectral bandwidths up to 8 GHz for both sensitive radio continuum imaging and spectral line surveys. Our new VLA observations of GCM0.253+0.016 exploit both of these capabilities to provide a comprehensive new study of the sub-parsec morphology, kinematics, and physical conditions of gas in this cloud. Our radio continuum observations allow for a more sensitive search for signs of ongoing star formation to determine whether indications of high-mass star formation in CMZ clouds may have been previously missed. With our molecular line data, we can examine kinematics of both low and high density gas in the cloud using NH_3, an abundant tracer of gas having densities greater than a few 10^3 cm^{-3}. The NH_3 observations are also sensitive to gas over a wide range of temperatures (from tens to hundreds of K), enabling us to investigate the full range of temperatures present in the pre-star-forming gas, and to map the temperature structure of that gas across the cloud. In this paper, we first present an analysis of the continuum emission and the morphology of the detected molecular species in GCM0.253+0.016, with detailed analyses of the kinematic and temperature structure to be presented in subsequent papers.

In Section 2, we describe the VLA observations and the procedures used to calibrate and image these data. We then present an overview of our study of GCM0.253+0.016, beginning with the properties of the continuum emission which are analyzed in Section 3. The morphology and kinematics of the molecular gas are subsequently analyzed in Section 4. In Section 5, we focus on emission from the 36.2 GHz CH_3OH line and present a catalog of more than 70 candidate collisionally excited masers. Finally, in Section 6, we discuss constraints on the amount and nature of ongoing star formation in this cloud.

2. OBSERVATIONS AND DATA CALIBRATION

The observations presented in this paper were made with the new WIDAR correlator of the VLA. The data were taken in two different frequency bands on two separate dates: in the Ka band (27–36 GHz) on 2012 January 13, and in the K band (24–25 GHz) on 2012 January 14, under project code 11B-210. Both observations used the hybrid DnC array configuration to compensate for the low altitude of the Galactic center as observed from the VLA site. In this paper we present only the observation of GCM0.253+0.016, however these data are part of a larger survey of the radio continuum and molecular line emission in CMZ clouds which will be described further in additional papers.

[7] The National Radio Astronomy Observatory is a facility of the National Science Foundation operated under cooperative agreement by Associated Universities, Inc.

Table 1
Observed Fields

Field	R.A. (J2000)	Decl. (J2000)	Array ConFigure	Int. Time (minutes)
K-band North	$17^h46^m08^s.95$	$-28°41'56''.8$	DnC	24.6
K-band South	$17^h46^m09^s.60$	$-28°43'24''.8$	DnC	24.9
Ka-band North	$17^h46^m08^s.44$	$-28°42'01''.0$	DnC	24.3
Ka-band South	$17^h46^m10^s.26$	$-28°43'07''.8$	DnC	24.4

2.1. Observation Setup

These observations employed the WIDAR correlator on the VLA in order to simultaneously observe both a wide spectral bandwidth for continuum studies and a large number of spectral lines. Observations in each band (K and Ka) are divided into two separate, continuous subbands of ∼0.84 GHz width which are each subdivided into seven spectral windows. In the K band, the subbands were centered on 24.054 and 25.375 GHz, and for the Ka band the subbands were centered on 27.515 and 36.35 GHz. The typical spectral resolution per spectral window is 250 kHz, with 512 channels per spectral window. However, for three spectral windows, covering (1) the NH_3 (1,1) and (2,2) lines and their hyperfine satellites, (2) the 36.6 GHz CH_3OH maser line, and (3) the CH_3CN $K = 2$–1 transitions, the resolution was increased (125 kHz, ∼1–1.5 km s^{-1}) to better resolve the line structure.

In order to map the majority of GCM0.253+0.016 in the K and Ka bands we used two pointings (see Table 1) oriented along the major axis of the cloud, which is elongated in declination. The total integration time for each field was ∼25 minutes. The distance between the pointings was $83''.5$ at K band and $70''.7$ at Ka band. Primary beam sizes range from ∼110″ at K band to ∼100″ and ∼75″ for the lower and upper frequencies observed at Ka band, respectively.

2.2. Calibration

The calibration of our K- and Ka-band VLA observations was performed using the CASA software provided by NRAO.[8] 3C286 was observed as the flux density calibrator, J1733-1304 was used as the bandpass calibrator, and J1744-3116 was used as the gain and phase calibrator. Reference pointing was performed every hour on the phase calibrator, which was observed every ∼25 minutes throughout the observations. In addition, at these higher VLA frequencies, corrections were made for the atmospheric opacity, which is determined from a mix of both actual weather data and a seasonal model using the *plotweather* task.

2.3. Imaging

The K- and Ka-band continuum and spectral data were imaged using the CLEAN task in CASA. As stated in Section 2.1, two pointings were observed to cover the cloud at both K and Ka bands, which were mosaicked together when imaging. Continuum data were obtained by flagging out the spectral lines and end channels. Briggs weighting with a robust parameter of 0.5 in order to balance the point-source resolution with the sensitivity, giving synthesized beams of $1''.59$–$2''.30$. The rms noise levels in the continuum images ranges from 29 to 55 μJy beam^{-1}. These values are generally about twice the theoretical rms noise levels of 17–27 μJy beam^{-1}, which may be due to the increased contributing emission coming from the Galactic plane. The largest angular scale to which the data are sensitive is ∼60″ at K band (or ∼2.4 pc) and ∼40″ (∼1.6 pc) at the higher-frequency Ka-band subband.

The K- and Ka-band spectral line data were also imaged using CLEAN. All lines were imaged individually, and continuum emission was subtracted using the CASA task *imcontsub*. The data were imaged at their intrinsic frequency resolution with no smoothing, and all spectral lines (except for the 36 GHz CH_3OH line) were imaged with natural weighting, resulting in synthesized beams which ranged from 1.58 to $1''.77$. For the 36 GHz CH_3OH line, which exhibited primarily point-source emission, the data were imaged using Briggs weighting with a robust parameter of 0.5. Beam parameters for all images are given in Table 2.

For the $NH_3(1, 1)$–$(6, 6)$ and HC_3N (3–2) and (4–3) transitions we used multiscale deconvolution to maximize sensitivity to extended emission in the cloud. The images were cleaned using beams with sizes of 0, 5, 20, and 80 pixels, and the parameter setting the relative weighting between these scales (0–80) was set to 0.6.

In the resulting multiscale images, "negative bowl" features indicative of missing extended flux were minimized, however the observations are still not sensitive to emission on scales larger than ∼1′. We did not use multiscale CLEAN for the $NH_3(7, 7)$–$(9, 9)$ and CH_3CN (2–1) lines, as it was not found to significantly improve the imaging of these weak lines, or for the 36 GHz CH_3OH line, for which the emission was primarily unresolved or on small spatial scales. The individual imaging parameters for each line can be found in Table 2. In general, the rms noise levels per channel range from 0.7 to 3.0 mJy beam^{-1} with the exception of CH_3OH (4–3). The typical rms levels for this transition varied, from 2.16 mJy beam^{-1} in maser-free channels to 116 in the brightest maser channel. These rms values are consistent with the theoretical rms values of 1.4 and 0.9 mJy beam^{-1} for channel widths of 0.125 and 0.250 MHz, respectively.

2.4. Self-calibration

For observations of the Ka-band (36 GHz) CH_3OH line, in which there are many strong point sources, we additionally self-calibrated the data. For each pointing, a bright CH_3OH point source with minimal additional emission surrounding the source was chosen for self-calibration. Here, the requirement that the point sources be relatively isolated was more important than that they be the strongest in the cube. Each pointing was first imaged using CLEAN with a small number of iterations, thus producing a map and model of the emission. This model was used by the CASA task gaincal for both phase and

[8] http://casa.nrao.edu/

Table 2
Continuum and Spectral Line Image Parameters

Continuum							
			——Synthesized Beam——				
Band	Center Frequency (GHz)	Bandwidth (GHz)	Major Axis (″)	Minor Axis (″)	Position Angle (°)	rms Noise (μJy b^{-1})	Peak Intensity (mJy b^{-1})
K (low)	24.054	0.86	2.30	1.97	70.8	47.6	1.135
K (high)	25.375	0.86	2.19	1.87	73.7	28.6	0.811
Ka (low)	27.515	0.86	2.21	1.87	73.7	30.0	0.636
Ka (high)	36.350	0.86	1.59	1.51	26.2	54.5	0.672

Spectral Line							
			——Synthesized Beam——				
Species+ Transition	Rest Frequency (GHz)	Channel Width (km s^{-1})	Major Axis (″)	Minor Axis (″)	Position Angle (°)	rms per Channel (mJy b^{-1})	Peak Intensity (mJy b^{-1})
NH_3(1, 1)	23.6945	1.58	2.83	2.58	66.9	1.6	40.2
NH_3(2, 2)	23.7226	1.58	2.83	2.58	66.9	1.2	39.9
NH_3(3, 3)	23.8701	3.14	2.81	2.56	66.8	1.9	232.4
NH_3(4, 4)	24.1394	3.10	2.75	2.55	70.0	0.9	26.2
NH_3(5, 5)	24.5329	3.05	2.70	2.52	69.9	0.8	15.3
NH_3(6, 6)	25.0560	2.99	2.66	2.44	71.1	1.2	18.3
NH_3(7, 7)	25.7152	2.91	2.59	2.37	69.1	0.7	9.3
HC_3N(3–2)	27.2943	2.75	3.15	2.45	22.9	1.5	43.2
NH_3(9, 9)	27.4779	2.73	2.89	2.33	45.5	1.1	11.9
CH_3OH(4–3)	36.1693	1.02	2.11	1.77	−2.6	2.16 (116)[a]	28174.0
HC_3N(4–3)	36.3923	2.06	1.96	1.77	15.4	3.0	40.6
CH_3CN(2–1)	36.7956	1.02	1.94	1.75	16.9	2.6	22.5

[a] The larger value is the rms noise in the channel containing the brightest maser, at $v = 30$ km s^{-1}.

amplitude calibrations. To begin with, phase-only self calibration was applied until the signal-to-noise improvement was no longer significant (2–3 iterations). After phase-only calibration, a single iteration of amplitude and phase self-calibration was performed. The self-calibration amplitude and phase solutions for this single channel were then applied to all of the channels in each pointing, and the pointings were jointly imaged using CLEAN as described above to form a final image.

3. CONTINUUM RESULTS AND ANALYSIS

Figure 1 shows the continuum emission associated with GCM0.253+0.016 at 24.1 GHz (upper left), 25.4 GHz (upper right), 27.5 GHz (lower left), and 36.4 GHz (lower right). Table 2 presents the properties of each of these continuum images, including the parameters of the synthesized beam and the rms noise level.

The radio continuum emission in the field of GCM0.253 +0.016 is fairly weak and typically extended over the same region in which gas and dust emission from the cloud has been detected (Kauffmann et al. 2013; Johnston et al. 2014; Rathborne et al. 2014b). Exceptions to this are several compact and brighter sources which, as previously noted by Rodríguez & Zapata (2013), are generally located outside of the majority of gas and dust emission associated with GCM0.253+0.016. Apart from these sources, the good coincidence in the spatial distribution and (as will be discussed further below), the morphology of the radio continuum and molecular gas emission, makes it likely that this continuum emission is truly associated with the GCM0.253+0.016 cloud, and does not just arise from other sources along this confused line of sight. As the continuum images have not been corrected for missing emission at large spatial scales with the addition of single dish data, some of the continuum emission may be resolved out, especially at the highest frequencies (36.4 GHz). At these frequencies, significant flux may be missing from structures larger than ~2–2.5 pc, affecting the calculations of spectral indices for these structures. The low-level, diffuse continuum emission, where it is detectable (mostly at 24.1 and 25.4 GHz) has a typical intensity of ~0.2 mJy beam^{-1}, with a few brighter clumps that extend up to ~0.7 mJy beam^{-1}. In the following section, we identify 10 regions that are a good representation of the continuum emission associated with this cloud and analyze the possible nature and origin of this emission.

3.1. Continuum Morphologies

The regions of continuum emission that we will evaluate here are shown in Figure 2. The regions are defined by a contour levels of 6 or 10 times the 24.1 GHz rms noise level of 30 μJy beam^{-1}) m depending on whether the regions are extended or compact, respectively. Table 3 summarizes the properties of these regions of continuum emission. In addition to presenting flux measurements for these regions from each of

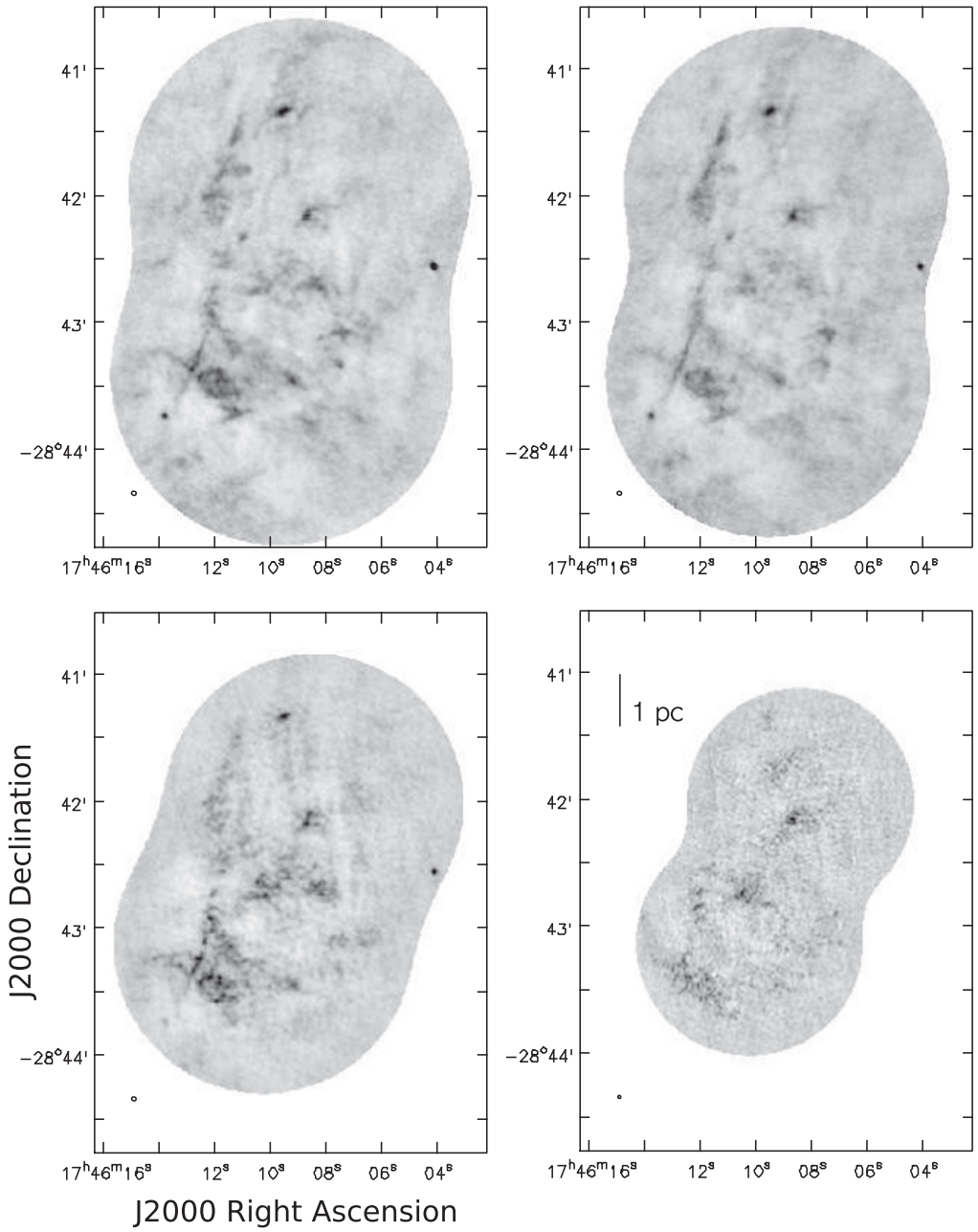

Figure 1. Continuum images at the four observation frequencies: 24.11 25.43, 27.45, and 36.4 GHz. All four sub-images were cleaned using the same restoring beam: 2.″295 × 1.″966, PA = 70.°8075, which corresponds to the beam size of the lowest frequency. The rms noise of the image at each of the four frequencies is 89.3, 63.1, 120, and 80.3 μJy beam^{-1}, respectively.

the VLA continuum images, we give the 90 GHz fluxes from both ALMA 12 m only images and single-dish-corrected ALMA images from Rathborne et al. (2014b).

Out of the 10 selected areas of interest, 4 regions (C2, C7, C8 and C9) are large and diffuse (>30″/1 pc across) and are primarily located in the eastern part of the field. Of these, C9, located in the southern part of the field, is the largest and brightest at 24.1 GHz. Contained within the 6σ contours of this region is a large elliptical or "shell"-like region having a long axis extent of ∼30″ as well as a long thin "filament" of emission running from northwest to southeast that lies tangential to the elliptical region, with the two intersecting at α(J2000) = 17^{h}46^{m}12.^{s}7, δ(2000) = −28°43′24″. This tangential filament is ∼35″ in length, corresponding to a physical size of 1.4 pc. Although some clumpy emission in the region of the shell and filament is detected above the noise in the 36.4 GHz image, the size of the region is on the order of the largest angular size at this frequency, and likely its emission has been suppressed. Both shell and filament are still faintly seen at 3 mm (Rathborne et al. 2014b), though their structure is not apparent at 230.9 GHz (Johnston et al. 2014).

Regions C7 and C8 have very similar structures and together form an apparent curved ridge of continuum emission across the cloud. While these two regions appear to fall along the same structure, they are separate at the 6σ level, and we treat them as separate regions. We note that like C9, the large-scale diffuse structure of these sources has likely been suppressed, and if there were a true connection between them, the present

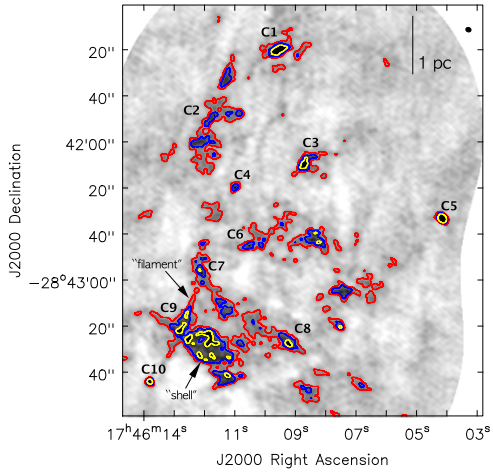

Figure 2. 1 GHz bandwidth continuum image at 24.1 GHz (top left panel in Figure 1) with 6, 10, and 15σ contour levels (from a non primary beam corrected rms of 3×10^{-5} Jy beam^{-1}) colorized as red, blue, and yellow, respectively. The continuum regions of interest are labeled as C1–10, using the specified contour levels stated in Table 3, depending on the compactness of the emission source. The region parameters, Lyman continuum flux, and spectral indices for these regions are also presented in Table 3.

data would not be sensitive to emission on that spatial scale. At 36.4 GHz, where the suppression of large-scale emission is most severe, only the brightest knots in these sources are detected above the noise at this frequency. The morphologies of these two regions are also reminiscent of that of the adjacent molecular gas in the clouds, as we will discuss further in Section 6.2.

Like C9, the continuum emission in the most northern diffuse region, C2, exhibits filamentary structure. The eastern edge of C2 forms a straight line that is parallel to the tangential filament in C9. The straight edge of C2 also extends northward to an additional clump that is separate in the 6σ contour levels. The total length of this linear feature, including the additional northern clump of emission, is ~46″ (1.85 pc), larger than the largest angular size scale of these data, suggesting that there could be extended emission connecting the two northern clumps that has been resolved out. This linear structure is apparent from 24.1 to 27.5 GHz, but it is absent at 36.4 GHz, likely because it falls in the less-sensitive outer regions of the primary beam at that frequency. As with the tangential filament C9, the linear structure of C2 is also present at 3 mm (Rathborne et al. 2014b). The morphology of this feature also appears to match that of an adjacent molecular gas filament seen in the NH_3 maps presented in Section 4.1. We discuss this relationship further in Section 6.2.

In addition to the extended continuum emission discussed above, there are several smaller regions of more compact continuum emission located inside of the confines of the cloud, as traced by the molecular gas emission. These continuum regions (C1, C3, C4, and C6) are relatively bright and also have counterparts at higher frequencies: all are detected in the 90 GHz ALMA image of Rathborne et al. (2014b). The remaining compact regions, C5, and 10, are the the brightest sources detected at 24.1 GHz, and lie outside of the boundaries of the cloud traced by the molecular gas emission. These sources are only marginally resolved by the VLA observations, and their peak intensities at 24 GHz are greater than 1.0 mJy beam^{-1}, and are larger than the peak intensities of other sources in the cloud (except C1) by at least a factor of 2. Although they lie near the edge of the Rathborne et al. (2014b) ALMA map, they are still detected at 90 GHz.

A number of the compact (<2″) sources were also identified by Rodríguez & Zapata (2013) using higher resolution VLA data. Their sources JVLA 1, 4, and 6 correspond to the previously discussed sources C5, C1 and C10, respectively. In addition, they detect a source (JVLA 5), that is part of our more extended source C7. As Rodríguez & Zapata (2013) also do not detect our C3, one of the stronger compact sources we detect in GCM0.253+0.016, it seems likely that these higher resolution data are more strongly affected by spatial filtering (the largest angular scale recoverable in the B-configuration VLA data of Rodríguez & Zapata 2013 should be around 10″). It may then be that several of the apparently compact sources they detect are simply the peaks of intrinsically more extended structures. Rodríguez & Zapata (2013) suggested these sources may represent high mass star formation associated with this cloud, in excess of that previously inferred by the presence of a single water maser in the northern part of the cloud. However, we note that in addition to several of their sources being associated with extended emission, all of them also lie outside of the dense molecular gas in the cloud, which is not what is expected if these sources are (proto)stellar in nature. We will discuss which of the compact sources we identify could be most consistent with star formation, based on their spectral indices, fluxes, morphologies, and relation to the molecular gas in the cloud, in Section 6.2.

3.2. Spectral Indices

To determine the nature of the radio continuum sources, and particularly to judge the amount of ongoing star formation in GCM0.253+0.016, the emission mechanism of the observed radio continuum in this cloud must be identified. We have calculated spectral indices for the 10 representative regions identified above. However, the VLA data alone are found to be insufficient for calculating accurate spectral indices, as the small range of radio frequencies probed by these observations does not provide a large lever arm for determining spectral indices, and the combination of the extended nature of much of the emission and the location of many sources near the edge of the primary beam appear to make the fluxes derived in the Ka band systematically low. For this reason, spectral indices are calculated using the fluxes at both K-band frequencies, and the 90 GHz fluxes from the ALMA continuum images of Rathborne et al. (2014b). Separate spectral indices are calculated using the both the images made from just the ALMA 12 m array, and the image that has been additionally corrected for missing extended flux via combination with single dish data. We expect that the true spectral indices likely fall between these two values, as our K-band data are sensitive to larger angular scales than the ALMA data, and should thus recover more flux than the ALMA 12 m only image, but less than the single-dish corrected ALMA image.

We find that the three sources at the center of the cloud (C3, C4, and C6) have consistently rising spectral indices, with α between 0.5 and 1.4, depending on whether the uncorrected or corrected ALMA fluxes are used in this calculation. The two sources outside of the cloud (C5 and C10) have consistently negative spectral indices: the spectral index of C5 is between −0.9 and −1.3, while the spectral index of C10 is between −0.3 and −0.7. This suggests that the emission from these two

Table 3
Continuum Regions

			Measured Flux (mJy)[a]						Spectral Index		
	Area	Cont.	24.1	25.4	27.5	36.4	90.0[b]	90.0[c]	(24–90 GHz)		log $N_{\rm Lyc}$
	(sq″)	Level	(GHz)	(GHz)	(GHz)	(GHz)	(GHz)	(GHz)	Uncorrected[b]	Corrected[c]	(phot s^{-1})
C1	35.7	10σ	4.6 ± 0.1	4.6 ± 0.2	4.2 ± 0.2	2.6 ± 0.1	3.1 ± 0.1	6.6 ± 0.3	−0.29 ± 0.01	0.27 ± 0.03	46.5
C2	279.1	6σ	18.8 ± 0.1	18.7 ± 0.1	15.6 ± 0.1	8.2 ± 0.2	10.5 ± 0.1	27.3 ± 0.3	−0.43 ± 0.01	0.28 ± 0.03	47.2
C3	27.6	10σ	2.3 ± 0.1	2.4 ± 0.1	2.1 ± 0.1	2.6 ± 0.2	5.9 ± 0.1	11.3 ± 0.6	0.68 ± 0.01	1.17 ± 0.05	45.9
C4	14.8	6σ	1.0 ± 0.1	0.9 ± 0.1	0.9 ± 0.1	0.5 ± 0.1	1.9 ± 0.1	4.2 ± 0.5	0.52 ± 0.09	1.1 ± 0.1	45.9
C5	16.1	10σ	6.3 ± 0.1	5.6 ± 0.2	4.0 ± 0.1	NA	1.0 ± 0.2	1.9 ± 0.4	−1.31 ± 0.03	−0.86 ± 0.05	…
C6	81.6	6σ	4.5 ± 0.1	4.2 ± 0.1	5.5 ± 0.1	6.1 ± 0.1	11.8 ± 0.1	26.6 ± 0.5	0.74 ± 0.07	1.34 ± 0.09	46.5
C7	161.9	6σ	10.7 ± 0.1	8.4 ± 0.2	10.1 ± 0.2	5.9 ± 0.2	8.3 ± 0.1	28.4 ± 0.4	−0.1 ± 0.15	0.8 ± 0.18	46.9
C8	164.2	6σ	8.4 ± 0.1	5.7 ± 0.1	6.3 ± 0.1	2.8 ± 0.1	6.4 ± 0.1	32.3 ± 0.5	−0.1 ± 0.17	1.1 ± 0.14	46.8
C9	521.8	6σ	43.4 ± 0.1	34.1 ± 0.2	37.7 ± 0.2	35.8 ± 0.2	24.4 ± 0.3	80.9 ± 0.3	−0.3 ± 0.25	0.6 ± 0.3	47.5
C10	7.7	10σ	1.6 ± 0.1	1.6 ± 0.2	NA	NA	0.6 ± 0.1	1.0 ± 0.1	−0.73 ± 0.03	−0.35 ± 0.01	…

[a] "NA" indicates this region was outside or near the edge of the field of view.
[b] Values from 3 mm ALMA-only image of Rathborne et al. (2014b).
[c] Values from single-dish-corrected ALMA image of Rathborne et al. (2014b).

sources is dominated by nonthermal processes. This is in good agreement with Rodríguez & Zapata (2013), who find that the spectral indices between 1.3 and 5.6 cm for C5 and C10 (their sources JVLA 1 and JVLA 6, respectively) are -0.9 ± 0.1 and -0.3 ± 0.2, respectively.

The remaining sources in GCM0.253+0.016 (C1, C2, C7, C8 and C9), the majority of which are extended, have nearly flat spectral indices (ranging from slightly negative to slightly positive in the uncorrected and corrected ALMA images, respectively), consistent with free–free emission. It has been suggested that this cloud could be a good target for detecting limb-brightened synchrotron emission from cosmic ray interactions, as it previously showed few signs of free–free continuum emission that would confuse the synchrotron signal (Jones 2014). However, our observations show that there is actually significant free–free emission in GCM0.253+0.016, and we do not see any indication of extended synchrotron emission. While we do detect continuum emission from the limb of GCM0.253+0.016, it appears thermal in nature, and is only present on the eastern edge of the cloud. While lower frequency observations might prove more optimal for searching for extended synchrotron emission from this cloud, GCM0.253+0.016 overlaps with a supernova remnant identified at 90 cm (Kassim & Frail 1996), and so ultimately this cloud is likely not an ideal candidate for detecting a synchrotron signal from cosmic ray interactions.

3.3. Thermal Emission from Ionizing Photons

For these sources and the sources with rising spectral indices we then calculate the Lyman-continuum photon rate to further constrain the properties of this thermal emission and its origin. Assuming the continuum emission in GCM0.253+0.016 is thermal in nature, caused by ionization from an external or embedded source, calculating the Lyman-continuum photon rate can give insight into the types of sources required to stimulate this emission. The number of ionizing Lyman-continuum photons needed to produce this emission can be calculated using the formulation of Mezger & Henderson (1967):

$$N_{\rm Lyc} = 1.301 \times 10^{49} \left(\frac{T_e}{\rm K}\right)^{-0.3} \left(\frac{S_\nu}{\rm Jy}\right) \left(\frac{D}{\rm kpc}\right)^2 \times \left(\ln\left(\frac{0.0499\ {\rm GHz}}{\nu}\right) + 1.5 \ln\left(\frac{T_e}{\rm K}\right)\right)^{-1} \quad (1)$$

where T_e is the electron temperature, assumed to be 10,000 K, S_ν is the flux density at a frequency ν in GHz, and D is the distance to the Galactic center, assumed to be 8.4 kpc. The Lyman-continuum photon rate was calculated for all 10 of the sources in Figure 2 (except for C5 and C10, which have a nonthermal spectral index at these frequencies) using the flux densities at 24.1 GHz, and are presented in column 12 of Table 3. The tabulated values of log N_L range from 45.9 to 47.5 with the largest values (>46.7) corresponding to the large diffuse regions. Assuming the stars producing this ionization are on the zero-age main sequence, which would be expected for a cloud undergoing star formation, this range of log N_L values would correspond to ionization by a single star with a spectral type of B1 to O9.5 (Panagia 1973). The three compact regions (C3, C4, and C6) located toward the center of the cloud would each be ionized with a star of spectral type B0.5. However, as these latter sources have apparently rising spectral indices, it is likely that the inferred Lyman continuum fluxes are either systematically overestimated (if these fluxes are contaminated with dust emission) or systematically underestimated (if these sources are in fact optically thick). As we will discuss further in Section 6.2, it is not possible to determine which is more likely.

4. MOLECULAR GAS MORPHOLOGY AND KINEMATICS

Not only does the large bandwidth of these VLA observations make possible the first sensitive radio continuum map of GCM0.253+0.016, it also enables a survey for spectral line emission in the cloud over a total bandwidth of ~4 GHz. In total, we detect and image 12 molecular lines from four species in

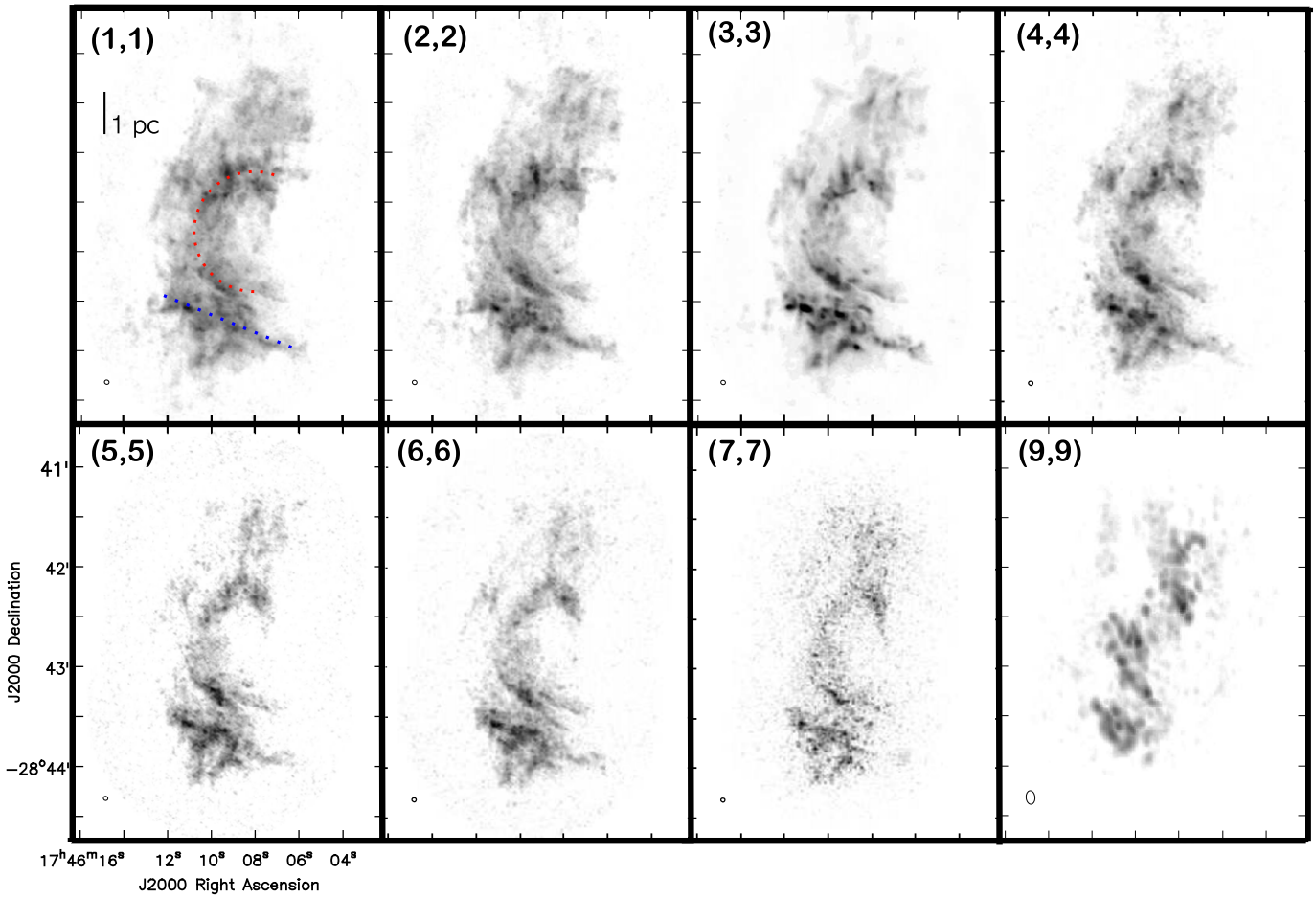

Figure 3. Maps of the maximum intensity over all velocities for the NH_3 (1, 1) to (9, 9) transitions. The morphological features referred to as the "C-arc" and the "tilted bar" are indicated in the (1, 1) map as a dotted red curve and a dotted blue line, respectively.

GCM0.253+0.016. With the high spectral (1–3 km s^{-1}) and spatial (3″ = 0.1 pc) resolution of these observations, it is possible to investigate the detailed morphology and kinematics of the molecular gas in GCM0.253+0.016, and for the first time to compare the distribution of the continuum emission from ionized and nonthermal structures with that of the molecular gas.

4.1. Morphology

The majority of the observed lines in GCM0.253+0.016 (8/12) are from ammonia (NH_3). Figure 3 shows the peak intensity of these eight observed transitions of NH_3: (J, K) = (1, 1), (2, 2), (3, 3), (4, 4), (5, 5), (6, 6), (7, 7), and (9, 9) (see Table 2 for image parameters). The first seven lines were imaged simultaneously with a single correlator setting at K band, while the (9, 9) was observed separately at Ka band. As the emission from the (9, 9) line is much weaker than the others, it was smoothed to improve the imaging signal to noise. The strongest observed line is the (3, 3) line (typically about twice as bright as the (1, 1) or (2, 2) lines). We take it to be generally representative of the distribution of NH_3 in this cloud given that, as can be seen in Figure 3, all of the observed NH_3 transitions exhibit very similar structure. In general, the emission is diffuse and filamentary throughout the cloud with many curved features. In the strongest lines (J, $K \leqslant 4$), much of the emission can be seen to be concentrated in a number of compact clumps. These clumps are most prominent in the (3, 3) line, likely in part because this line is the strongest. The clumps have typical brightness temperatures of 10–60 K in the (3, 3) line which is consistent with thermal emission, although (3, 3) masers have been previously suggested to exist in CMZ clouds (Martin-Pintado et al. 1999).

In our NH_3 maps, we identify two primary features of the morphology of GCM0.253+0.016. emission. The first is an apparently "C" shaped arc located near the center of the cloud (hereafter "C-arc"). The "C-arc" extends roughly 90″ (or 3.7 pc) in decl. (from −28°42′00″ to −28°43′30″, at an R.A. of ∼17^{h}46^{m}08^s). The "C-arc" structure can be seen in recent millimeter spectral line studies of this cloud using ALMA (Higuchi et al. 2014; Rathborne et al. 2015), and the SMA (Johnston et al. 2014). It is suggested by Higuchi et al. (2014) that this feature is the remnant of a recent collision between GCM0.253+0.016 and a smaller cloud. The "C-arc" has roughly the same brightness as emission in other regions of the cloud in the (1, 1) and (2, 2) lines (likely because the bulk of the emission in these lines is optically thick, as will be discussed further in a subsequent paper) but it is prominent in the higher-excitation lines of NH_3. Intriguingly, this arc follows very well the direction of the magnetic vectors inferred from recent polarization studies of this cloud (Pillai et al. 2015).

The second feature is a "tilted bar" below the "C-arc," beginning on the eastern side of the cloud at a declination of −28°43′.5 and spanning nearly the entire width of the cloud in right ascension. In lines of NH_3 (3, 3) and above, this region

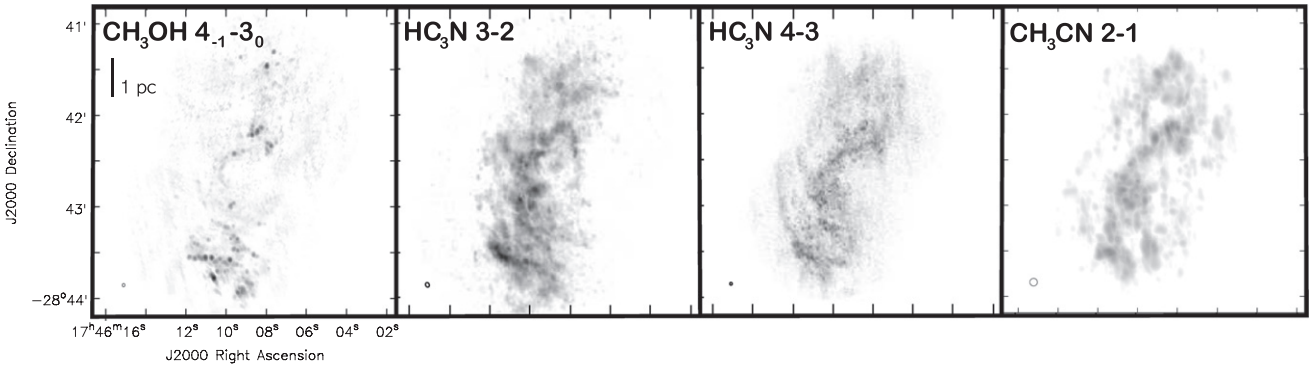

Figure 4. Maps of the maximum intensity over all velocities. Left: CH_3OH 4_{-1}–3_0 line. Middle-left: HC_3N 3–2 line. Middle-right: HC_3N 4–3 line. Right: the blended CH_3CN 2_k–1_k doublet in GCM0.253+0.016.

and the adjacent southern portion of the C-arc are the sources of the most intense NH_3 emission in GCM0.253+0.016, and this tilted bar contains the bulk of the brightest clumps seen in the NH_3 (3, 3) line. In addition to the prominent tilted bar in the southern half of the cloud, there are also a number of weaker linear emission features in both the north and south of the cloud. The easiest to identify in the NH_3 maximum emission maps is a feature on the eastern edge of the cloud above the "C-arc." It is narrow, extending from a decl. of 41.″25 to 41.″75, and is best seen in the $K \leqslant 4$ lines. The southern edge of the "C-arc" and the southwestern "tail" of the bar also form nearly linear elongations. We will return to a discussion of the linear emission features in GCM0.253+0.016 and how they relate to the linear radio continuum features and the HCO^+ absorption filaments identified by Bally et al. (2014) in Section 6.2.

In addition to the NH_3 lines, in the Ka band, we also detect the (4_{-1}–3_0) line of CH_3OH and the (3–2) and (4–3) transitions of HC_3N and the (2–1) doublet of CH_3CN, maximum emission maps of which are shown in Figure 4. The CH_3OH line shows the most striking difference in morphology compared to all other lines imaged in this cloud: it is primarily composed of emission from dozens of discrete point sources. More than half of these point sources are located in the southern bar. The majority of the observed point sources have brightness temperatures >400 K and are likely masers; we discuss the nature of the observed 36.2 GHz CH_3OH emission sources in GCM0.253+0.016 further in Section 5. Overall, these molecules trace the same general structure as seen in NH_3: the "C-arc" is clearly visible, and the southern bar can be seen in the CH_3OH and HC_3N lines, though it is less prominent in the faint line CH_3CN line. However, the HC_3N and CH_3CN images both exhibit stronger emission at the center of the cloud (along the "C-arc," between a declination of −28°42′.5 and −28°43′) than is seen in either the NH_3 or CH_3OH images. As can be seen in millimeter continuum images (Johnston et al. 2014; Rathborne et al. 2014b), the center of the cloud is also where the dust continuum emission is strongest, suggesting that it is the location of the densest gas.

4.2. Kinematics

Although GCM0.253+0.016 may be considered quiescent in terms of its (lack of) ongoing star formation activity, its kinematics are much more active. In the left panel of Figure 5, we show a Moment 1 map of the intensity-weighted velocity from the NH_3 (3, 3) line, which is the brightest of the observed NH_3 transitions. The map was made by limiting the emission spatially to the region previously identified during the initial CLEAN, and by using a threshold of 2–3 times the rms noise value for the spectral line. Emission toward the cloud in the (3, 3) line spans velocities from −10 to 90 km s^{-1} (with weak emission, which does not contribute significantly to the average values in this figure, extending to velocities as low as −40 km s^{-1}). The lowest velocities (−10 to +20 km s^{-1}) in the cloud generally fall in the northern region of the cloud, while the southern region of the cloud is characterized by gas in the range of 20–60 km s^{-1}. The highest velocities (70–90 km s^{-1}) are primarily confined to a region at the southwest edge of GCM0.253+0.016, which has been suggested by Rathborne et al. (2014a) and Johnston et al. (2014) to be a separate cloud which may or may not be related to the main cloud.

A similarly constructed map of the intensity-weighted velocity dispersion (Moment 2) in the same line (Figure 5, middle panel) shows dispersions ranging from 2 to 30 km s^{-1}. However, the largest of these velocity dispersions ($\Delta v > 20$ km s^{-1}) may be misleading due to the presence of multiple components along some lines of sight. This complicated velocity structure of GCM0.253+0.016 is represented in three example spectra shown in the rightmost panel of Figure 5. There are multiple velocity components in the northern part of the cloud along the same line of sight that confuse this analysis, causing the velocity dispersion to represent a combination of the width of these components and their separation. An example of this is shown in spectrum A, a triple profile spectrum with intensity peaks around −15, 0, and 30 km s^{-1}. Areas with multiple velocity components can be similarly poorly represented in the Moment 1 map: often the average velocity lies between velocity peaks, and is located at a velocity which little or no gas is present. Spectra toward the center of the Brick, along the "C-arc," discussed in Section 4.1, show a double peak profile as can be seen in spectrum B of Figure 5. The peak intensities of the profiles presented in spectrum B fall at velocities of 10–15 and 35–40 km s^{-1}. This kinematic structure is typical for regions along the "C-arc." The southern part of GCM0.253+0.016 has single line profiles (see spectrum C), with velocities greater than 30 km s^{-1}, that typically represent the brightest emission in the cloud, with brightness temperatures at least 2–3 times the emission from other parts of the cloud.

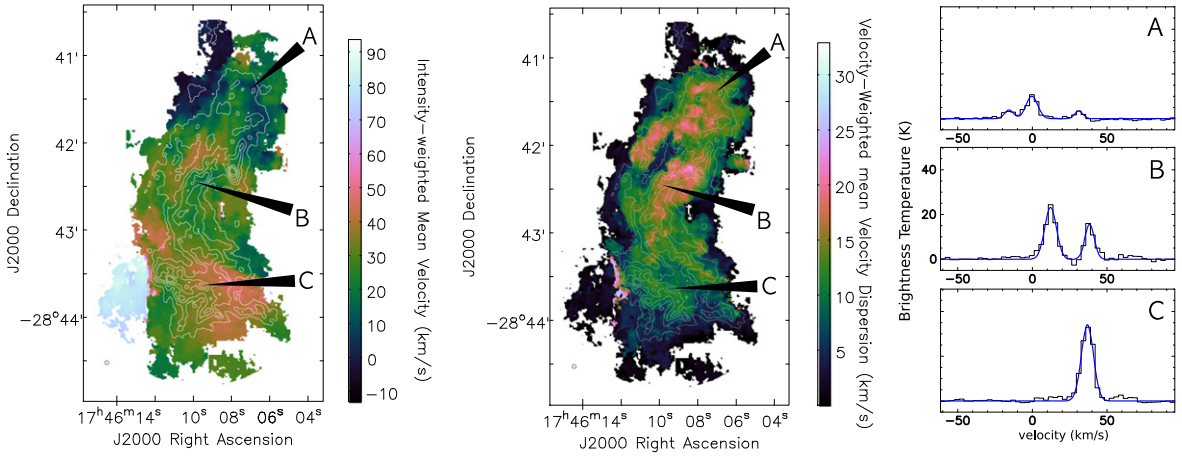

Figure 5. Left: a map of the intensity-weighted velocity (moment 1) from the NH_3 (3, 3) line. Center: a map of the intensity-weighted velocity dispersion (moment 2) from the NH_3 (3, 3) line. Overlaid on both the moment 1 and 2 images are contours of the integrated value of the spectrum (moment 0). Right: spectra extracted from the NH_3 (3, 3) cube from three positions in GCM0.253+0.016.

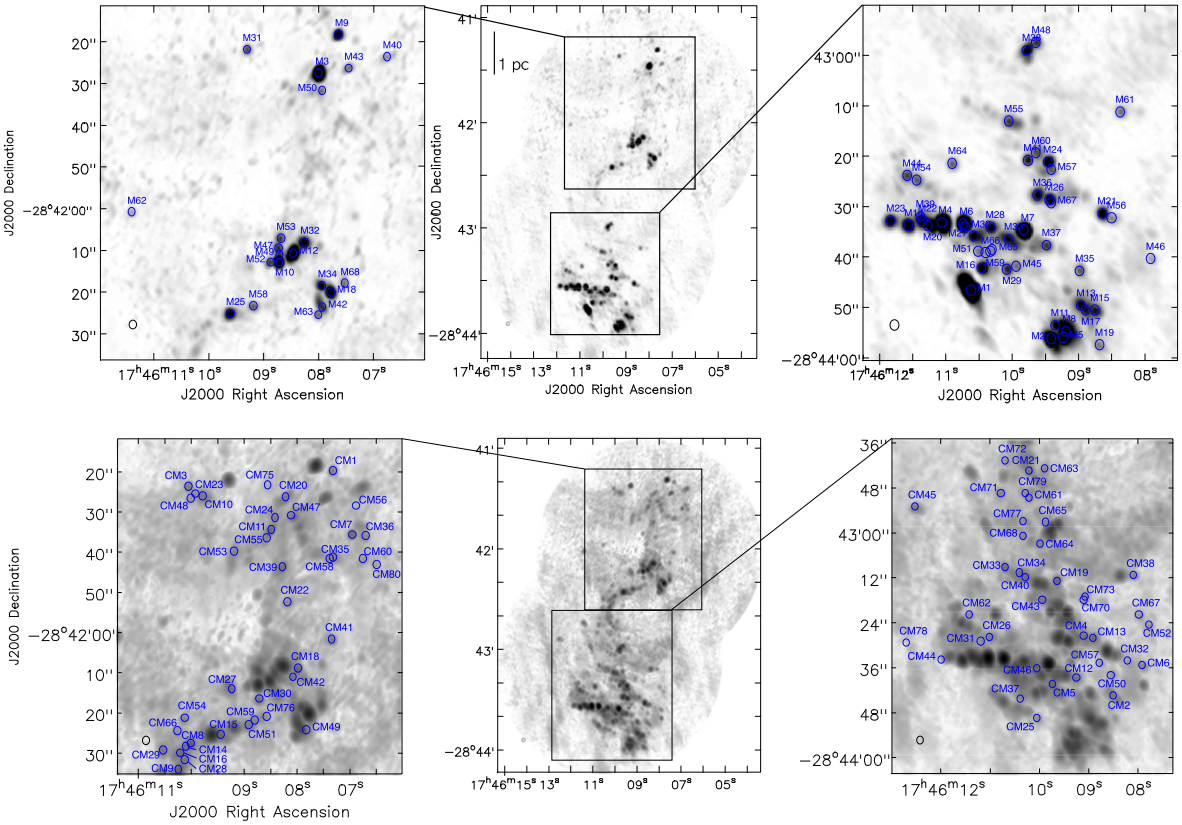

Figure 6. Maps of the peak 36.2 GHz CH_3OH emission detected in GCM0.253+0.016. Top: a map of the CH_3OH sources which we have determined to be masers. Sources are labeled M1-M68, and their properties are given in Table 4. Bottom: a map of the CH_3OH sources which cannot yet be determined to be masers, and are cataloged as maser candidates. In order to make visible the emission from these weaker sources, noisier channels in the cube which contain the two brightest masers (corresponding to velocities of 28–32 km s^{-1}) were not used to construct this image. The candidate sources are labeled CM1-CM80, and their properties are reported in Table 5.

5. WIDESPREAD 36.2 GHZ CH_3OH MASER EMISSION

As discussed in Section 4.1, the 36.2 GHz CH_3OH (4_{-1}–3_0) line exhibits the most unique morphology of all of the spectral lines we observe. While all of the other lines exhibit extended, filamentary, and clumpy structure, the CH_3OH emission lacks extended structure, and consists nearly entirely of discrete point sources. We detect dozens of these point sources, shown in Figure 6, a maximum intensity map of the CH_3OH emission within the cloud. While the distribution of sources spans the entire cloud, the majority of the sources, including nearly all of the brightest sources, are concentrated in the southern part of GCM0.253+0.016.

The point-like nature of the bulk of the CH_3OH emission is consistent with the 4_{-1}–3_0 transition being a well-documented "class I" or collisionally excited CH_3OH maser (Morimoto et al. 1985; Menten 1991; Slysh et al. 1994; Sjouwerman et al. 2010). In general, masers in this line are observed to trace

Table 4
36 GHz CH_3OH Masers

ID	Maser Name	R.A. (HH:MM:SS.s)	Decl. (DD:MM:SS.s)	Velocity (km s^{-1})	FWHM (km s^{-1})	I_{peak} (Jy beam^{-1})	Flux (Jy km s^{-1})	T_B (K)	Resolved?
M1	G0.2398299 + 0.0034302	17:46:10.62	−28:43:46.6	30.447	3.184	76.212	333.646	19269	YES
M2	G0.2352551 + 0.0058162	17:46:09.41	−28:43:56.2	38.735	3.484	32.446	152.436	8203	YES
M3	G0.2678706 + 0.0317273	17:46:08.00	−28:41:27.4	30.447	1.836	27.686	76.003	7000	NO
M4	G0.2438565 + 0.0040277	17:46:11.06	−28:43:33.1	35.627	2.912	21.630	85.486	5468	NO
M5	G0.2349796 + 0.0064290	17:46:09.23	−28:43:55.9	40.807	4.172	20.860	148.052	5274	YES
M6	G0.2431785 + 0.0049810	17:46:10.74	−28:43:33.4	21.124	2.981	20.305	57.793	5133	NO
M7	G0.2411601 + 0.0076552	17:46:09.82	−28:43:34.6	33.555	4.162	19.237	60.459	4863	NO
M8	G0.2351776 + 0.0067447	17:46:09.19	−28:43:54.7	39.771	3.814	17.971	130.015	4543	YES
M9	G0.2693832 + 0.0342102	17:46:07.64	−28:41:18.1	6.620	6.638	14.104	86.632	3565	NO
M10	G0.2584673 + 0.0229753	17:46:08.71	−28:42:12.7	31.483	2.249	10.252	29.481	2592	NO
M11	G0.2357657 + 0.0064198	17:46:09.35	−28:43:53.5	35.627	5.246	10.178	79.186	2573	NO
M12	G0.2584886 + 0.0240620	17:46:08.46	−28:42:10.6	39.771	4.477	9.906	53.927	2504	YES
M13	G0.2359542 + 0.0081933	17:46:08.96	−28:43:49.6	36.663	3.958	9.344	63.827	2362	YES
M14	G0.2446676 + 0.0023749	17:46:11.56	−28:43:33.7	27.339	2.525	8.720	27.893	2204	NO
M15	G0.2353505 + 0.0087040	17:46:08.75	−28:43:50.5	38.735	3.241	8.510	52.511	2151	YES
M16	G0.2405942 + 0.0045786	17:46:10.46	−28:43:42.1	29.411	3.563	8.304	29.414	2099	YES
M17	G0.2356106 + 0.0082769	17:46:08.89	−28:43:50.5	39.771	3.778	8.233	45.093	2081	NO
M18	G0.2549814 + 0.0248543	17:46:07.77	−28:42:19.9	19.052	5.856	7.682	51.912	1942	YES
M19	G0.2335835 + 0.0079207	17:46:08.68	−28:43:57.4	42.879	3.324	6.400	38.649	1618	NO
M20	G0.2440175 + 0.0034427	17:46:11.27	−28:43:33.7	33.555	5.959	6.225	36.388	1573	NO
M21	G0.2396891 + 0.0118337	17:46:08.64	−28:43:31.3	49.095	4.186	6.195	21.655	1566	NO
M22	G0.2444911 + 0.0031456	17:46:11.35	−28:43:32.8	33.555	3.669	6.150	32.977	1554	NO
M23	G0.2454012 + 0.0016506	17:46:11.83	−28:43:32.8	31.483	2.822	6.107	24.441	1543	YES
M24	G0.2436696 + 0.0107445	17:46:09.46	−28:43:21.1	49.095	2.670	5.156	18.498	1303	NO
M25	G0.2572398 + 0.0184216	17:46:09.60	−28:42:25.0	7.656	5.076	5.124	33.197	1295	YES
M26	G0.2418468 + 0.0097322	17:46:09.44	−28:43:28.6	44.951	2.828	4.877	16.039	1233	NO
M27	G0.2423057 + 0.0051327	17:46:10.58	−28:43:35.8	31.483	6.288	4.842	42.715	1224	YES
M28	G0.2422560 + 0.0061758	17:46:10.33	−28:43:34.0	35.627	5.536	4.668	42.038	1180	YES
M29	G0.2397862 + 0.0057454	17:46:10.08	−28:43:42.4	27.339	3.447	4.482	19.467	1133	YES
M30	G0.2429928 + 0.0049656	17:46:10.71	−28:43:34.0	25.267	5.322	4.395	27.276	1111	YES
M31	G0.2716946 + 0.0284917	17:46:09.30	−28:41:21.7	−2.704	2.087	4.354	13.012	1100	NO
M32	G0.2587389 + 0.0250928	17:46:08.25	−28:42:07.9	34.591	3.461	4.336	27.130	1096	YES
M33	G0.2411665 + 0.0066833	17:46:10.05	−28:43:36.4	40.807	5.608	4.201	67.957	1062	YES
M34	G0.2556408 + 0.0245727	17:46:07.93	−28:42:18.4	39.771	7.755	3.710	29.827	937	YES
M35	G0.2376346 + 0.0091190	17:46:08.98	−28:43:42.7	37.699	1.279	3.699	7.069	935	NO
M36	G0.2424071 + 0.0092927	17:46:09.62	−28:43:27.7	47.023	3.272	3.621	20.174	915	YES
M37	G0.2397982 + 0.0082897	17:46:09.48	−28:43:37.6	43.915	4.043	3.486	33.611	881	YES
M38	G0.2495436 + 0.0129548	17:46:09.78	−28:42:58.9	19.052	3.634	3.421	21.531	864	YES
M39	G0.2447480 + 0.0032044	17:46:11.38	−28:43:31.9	30.447	4.930	3.377	20.993	853	YES
M40	G0.2664108 + 0.0362072	17:46:06.75	−28:41:23.5	3.512	2.686	2.898	11.934	732	YES
M41	G0.2443042 + 0.0098623	17:46:09.76	−28:43:20.8	50.131	1.878	2.850	6.041	720	YES
M42	G0.2544308 + 0.0238358	17:46:07.93	−28:42:23.5	42.879	4.374	2.814	22.516	711	YES
M43	G0.2671146 + 0.0336096	17:46:07.45	−28:41:26.2	9.728	1.446	2.714	6.569	686	NO
M44	G0.2470599 + 0.0037337	17:46:11.58	−28:43:23.8	35.627	2.917	2.650	10.509	670	YES
M45	G0.2396685 + 0.0062592	17:46:09.94	−28:43:41.8	33.555	3.344	2.578	17.679	651	YES
M46	G0.2361667 + 0.0128114	17:46:07.91	−28:43:40.3	48.059	1.179	2.549	4.716	644	NO
M47	G0.2592935 + 0.0233809	17:46:08.73	−28:42:09.4	41.843	2.275	2.392	6.557	604	NO
M48	G0.2496394 + 0.0135987	17:46:09.64	−28:42:57.4	35.627	1.599	2.382	4.899	602	NO
M49	G0.2588943 + 0.0232354	17:46:08.71	−28:42:10.9	40.807	3.613	2.340	12.201	591	NO
M50	G0.2667441 + 0.0313341	17:46:07.93	−28:41:31.6	31.483	1.821	2.328	4.342	588	NO
M51	G0.2414639 + 0.0049129	17:46:10.51	−28:43:38.8	33.555	5.188	2.203	14.952	556	NO
M52	G0.2587707 + 0.0224769	17:46:08.87	−28:42:12.7	39.771	3.374	2.190	7.639	553	NO
M53	G0.2597762 + 0.0238700	17:46:08.68	−28:42:07.0	39.771	2.907	2.180	6.395	551	NO
M54	G0.2465863 + 0.0040308	17:46:11.44	−28:43:24.7	39.771	5.857	2.137	10.270	540	NO
M55	G0.2467184 + 0.0100636	17:46:10.05	−28:43:13.0	33.555	2.486	2.110	13.584	533	YES
M56	G0.2392155 + 0.0121308	17:46:08.50	−28:43:32.2	50.131	5.607	2.022	14.468	511	NO
M57	G0.2432270 + 0.0106702	17:46:09.41	−28:43:22.6	35.627	2.587	2.016	10.836	509	YES
M58	G0.2568865 + 0.0199632	17:46:09.19	−28:42:23.2	9.728	2.790	2.016	7.985	509	NO
M59	G0.2411171 + 0.0054824	17:46:10.33	−28:43:38.8	38.735	5.613	1.980	25.949	500	YES
M60	G0.2444434 + 0.0104350	17:46:09.64	−28:43:19.3	36.663	3.288	1.977	16.399	499	YES
M61	G0.2439377 + 0.0155918	17:46:08.37	−28:43:11.2	37.699	1.277	1.958	2.131	495	NO
M62	G0.2664301 + 0.0163067	17:46:11.40	−28:42:00.7	−4.776	1.256	1.871	2.169	473	NO
M63	G0.2541338 + 0.0233622	17:46:08.00	−28:42:25.3	47.023	4.585	1.859	7.060	470	NO

Table 4
(Continued)

ID	Maser Name	R.A. (HH:MM:SS.s)	Decl. (DD:MM:SS.s)	Velocity (km s^{-1})	FWHM (km s^{-1})	I_{peak} (Jy beam^{-1})	Flux (Jy km s^{-1})	T_B (K)	Resolved?
M64	G0.2463291 + 0.0062161	17:46:10.90	−28:43:21.4	43.915	1.510	1.802	4.377	455	NO
M65	G0.2411450 + 0.0055969	17:46:10.30	−28:43:38.5	43.915	2.842	1.728	9.365	436	NO
M66	G0.2411760 + 0.0052255	17:46:10.40	−28:43:39.1	27.339	4.334	1.682	6.055	425	NO
M67	G0.2416611 + 0.0097167	17:46:09.41	−28:43:29.2	49.095	3.599	1.665	7.314	420	NO
M68	G0.2550027 + 0.0259409	17:46:07.52	−28:42:17.8	32.519	2.458	1.640	6.657	414	NO

shocks: they are found in outflows in early stages of both low and high-mass star formation (Kurtz et al. 2004; Chen et al. 2009; Kalenskii et al. 2010), around expanding ultracompact H II regions (Voronkov et al. 2010), as well as in the shells of expanding supernova remnants interacting with molecular clouds (Pihlström et al. 2014). Although within the plane of our Galaxy, class I CH_3OH masers have thus far been observed to be associated nearly exclusively with early stages of star formation, in the CMZ this association is less clear. In Sgr B2, roughly a dozen 44 GHz (7_0–6_1) class I masers are observed, many of which are not near known sites of star formation in the cloud (Mehringer & Menten 1997). These masers have been suggested to be induced by large-scale shocks from a cloud–cloud collision, which has also been suggested to excite 36 GHz masers observed near Sgr A (Sjouwerman et al. 2010). Mehringer & Menten (1997) also observe quasithermal emission in the 44 GHz line in Sgr B2, which is interpreted as originating in denser gas in which the maser has been quenched (Menten 1991). More recently, Yusef-Zadeh et al. (2013a) find emission from the 36 GHz line to be widespread in the CMZ. The large number (>350) of these sources is perhaps not surprising, as models (e.g., Cragg et al. 1992) suggest that the 36 and 44 GHz CH_3OH transitions are the easiest of 28 known and predicted class I CH_3OH masers to excite (though new class I CH_3OH masers continue to be predicted and detected; Voronkov et al. 2012; Yanagida et al. 2014). The widespread distribution of these sources in the absence of other tracers of widespread star formation leads Yusef-Zadeh et al. (2013a) to dismiss this as the likely origin of the CH_3OH emission (nor is it likely to be due to supernova interactions, as the sources are not confined to the few known supernova remnants in the region). Instead, Yusef-Zadeh et al. (2013a) suggest that the enhanced CH_3OH abundances in in the CMZ are a result of desorption from grains by cosmic rays. We discuss the merits of both a shock and cosmic ray model for giving rise to these CH_3OH sources in Section 6.1. Ultimately however, the low spectral resolution (∼17 km s^{-1}) of the Yusef-Zadeh et al. (2013a) survey does not allow for the 36 GHz sources to be positively confirmed to be masers.

5.1. Identification of Maser Candidates and Source Catalog

Although we observe the CH_3OH line with similar spatial resolution as Yusef-Zadeh et al. (2013a), our spectral resolution of ∼1 km s^{-1} is better able to discern whether these sources have nonthermal brightness temperatures. In order to more quantitatively analyze the observed CH_3OH emission in GCM0.253+0.016 and determine whether the observed sources are masers, we have produced an initial catalog listing the properties of the strongest detected sources.

The CH_3OH emission seen in Figure 6 is clustered together both spatially and spectrally. This clustering makes manually distinguishing between individual sources difficult. In order to examine these complicated fields, we adopt a version of the source detection algorithm *Clumpfind* (Williams et al. 1994) which distinguishes between sources that may partially overlap in position or velocity. *Clumpfind* identifies local maxima, then examines the emission surrounding the maxima both spatially and spectrally to determine the boundaries of the source. No assumptions about the clump geometry, neither spatially or spectrally, are made during processing by the algorithm. *Clumpfind* produces a list of maser candidate clumps with uniform criteria. The output of *Clumpfind* is then used to construct the catalog. Since a significant portion of the maser emission lies near the edge of the observed Ka-band field, a primary beam correction was applied while calculating the properties of the sources found by *Clumpfind*. Clumpfind searched for emission down to six times the rms noise in each channel.

Our *Clumpfind* analysis of GCM0.253+0.016 yields 383 CH_3OH clumps with a brightness above six times the rms noise. However, in order to remove the possibility of false detections, we required sources to have a brightness greater then 10 times the rms noise in their spectral channel in order to be included in the catalog; 195 CH_3OH clumps meet this criterion, which is a conservative cut-off that ensures that we are examining masers and not artifacts from several of the extremely bright masers in the field. However, as a result the final catalog of sources is incomplete below a flux of 1.0 Jy (the largest residual in the cube after removing the *Clumpfind*-detected sources), with the incompleteness being most significant near the velocity range of the brightest masers. Additionally, we make a total flux cut at 0.3 Jy, below which emission structure in the image begins to become significantly compromised by the missing flux on large scales. This removes 47 more sources, leaving a total of 148 detected CH_3OH point sources.

These *Clumpfind* sources are then divided into two catalogs: masers, and candidate masers. Of the 148 cataloged point sources, 68 have brightness temperatures >400 K, in excess of the highest gas temperatures suggested to exist in this cloud (∼325 K, Mills & Morris 2013; Johnston et al. 2014). This indicates that they are likely nonthermal, and we classify them as masers. Their properties, including the FWHM line width and peak brightness temperature, are given in Table 4. The remaining 80 sources have brightness temperatures that could be thermal, and so cannot yet be confirmed to be masers, given the limited spatial and spectral resolution of these data. Their properties are given in Table 5. Spectra for all of the cataloged CH_3OH sources, both masers and candidates, are presented in Figures 7 and 8. Due to the spatial and spectral clustering of the sources, the spectrum of a candidate may show other peaks from bright masers located nearby. To aid in identification of

Table 5
36 GHz CH_3OH Maser Candidates

ID	Candidate Name	R.A. (HH:MM:SS.s)	Decl. (DD:MM:SS.s)	Velocity (km s^{-1})	FWHM (km s^{-1})	I_{peak} (Jy beam^{-1})	Flux (Jy km s^{-1})	T_B K	Resolved?
CM1	G0.2684202 + 0.0349905	17:46:07.32	−28:41:19.6	27.339	1.126	1.565	1.958	395	NO
CM2	G0.2365820 + 0.0105272	17:46:08.50	−28:43:43.3	42.879	1.494	1.555	7.302	393	YES
CM3	G0.2726984 + 0.0258817	17:46:10.05	−28:41:23.5	1.440	1.211	1.472	2.500	372	NO
CM4	G0.2414813 + 0.0109734	17:46:09.10	−28:43:27.4	40.807	5.521	1.450	13.575	366	YES
CM5	G0.2396343 + 0.0071166	17:46:09.73	−28:43:40.3	35.627	8.515	1.433	17.606	362	YES
CM6	G0.2373767 + 0.0135482	17:46:07.91	−28:43:35.2	55.311	4.992	1.332	7.914	336	YES
CM7	G0.2639542 + 0.0338325	17:46:06.95	−28:41:35.5	25.267	1.212	1.274	2.257	322	NO
CM8	G0.2574507 + 0.0167933	17:46:10.01	−28:42:27.4	7.656	4.640	1.262	5.075	318	NO
CM9	G0.2563183 + 0.0151279	17:46:10.24	−28:42:34.0	14.908	5.059	1.248	18.386	315	YES
CM10	G0.2716086 + 0.0263896	17:46:09.78	−28:41:25.9	−0.632	4.520	1.147	10.161	289	NO
CM11	G0.2671442 + 0.0292350	17:46:08.48	−28:41:34.3	12.836	4.286	1.139	6.661	287	NO
CM12	G0.2391512 + 0.0088715	17:46:09.25	−28:43:38.5	36.663	1.063	1.117	1.160	282	NO
CM13	G0.2409922 + 0.0114562	17:46:08.91	−28:43:28.0	49.095	3.557	1.104	6.213	279	YES
CM14	G0.2572715 + 0.0158058	17:46:10.21	−28:42:29.8	16.980	4.448	1.074	9.304	271	YES
CM15	G0.2568652 + 0.0188767	17:46:09.44	−28:42:25.3	10.764	5.441	1.065	9.814	269	YES
CM16	G0.2574106 + 0.0163785	17:46:10.10	−28:42:28.3	11.800	4.718	1.050	6.166	265	NO
CM17	G0.2403644 + 0.0091223	17:46:09.37	−28:43:34.3	33.555	<1.036	1.020	0.928	257	NO
CM18	G0.2580051 + 0.0258172	17:46:07.98	−28:42:08.8	25.267	4.792	0.993	4.854	251	YES
CM19	G0.2460093 + 0.0113884	17:46:09.64	−28:43:12.7	35.627	2.245	0.992	3.101	250	YES
CM20	G0.2685456 + 0.0312597	17:46:08.21	−28:41:26.2	9.728	2.218	0.934	5.817	236	YES
CM21	G0.2540684 + 0.0138556	17:46:10.21	−28:42:43.3	16.980	4.247	0.895	12.616	226	YES
CM22	G0.2623100 + 0.0275602	17:46:08.18	−28:41:52.3	28.375	1.281	0.883	1.387	223	NO
CM23	G0.2720112 + 0.0260490	17:46:09.92	−28:41:25.3	2.476	5.335	0.877	3.608	221	NO
CM24	G0.2677259 + 0.0298821	17:46:08.41	−28:41:31.3	5.584	6.154	0.853	3.208	215	NO
CM25	G0.2381058 + 0.0048198	17:46:10.05	−28:43:49.3	27.339	1.216	0.811	1.138	205	NO
CM26	G0.2450510 + 0.0049501	17:46:11.01	−28:43:27.7	23.195	3.486	0.781	5.021	197	YES
CM27	G0.2591797 + 0.0211644	17:46:09.23	−28:42:13.9	43.915	2.376	0.776	3.477	196	NO
CM28	G0.2566710 + 0.0158306	17:46:10.12	−28:42:31.6	11.800	4.636	0.776	6.625	196	NO
CM29	G0.2580207 + 0.0148956	17:46:10.53	−28:42:29.2	34.591	1.210	0.751	0.889	189	NO
CM30	G0.2576131 + 0.0224553	17:46:08.71	−28:42:16.3	47.023	1.371	0.746	1.814	188	NO
CM31	G0.2451130 + 0.0042073	17:46:11.19	−28:43:28.9	28.375	2.262	0.743	2.622	187	YES
CM32	G0.2382249 + 0.0127961	17:46:08.21	−28:43:34.0	56.347	5.856	0.734	7.584	185	YES
CM33	G0.2488573 + 0.0086336	17:46:10.69	−28:43:09.1	35.627	1.670	0.733	1.084	185	NO
CM34	G0.2479380 + 0.0093424	17:46:10.40	−28:43:10.6	36.663	2.849	0.713	1.683	180	NO
CM35	G0.2632957 + 0.0318697	17:46:07.32	−28:41:41.2	27.339	1.717	0.700	2.202	176	NO
CM36	G0.2634060 + 0.0345724	17:46:06.70	−28:41:35.8	1.440	3.715	0.700	3.895	176	YES
CM37	G0.2399226 + 0.0045600	17:46:10.38	−28:43:44.2	27.339	3.211	0.696	3.186	175	YES
CM38	G0.2434175 + 0.0164461	17:46:08.09	−28:43:11.2	45.987	1.161	0.690	1.192	174	NO
CM39	G0.2645475 + 0.0285323	17:46:08.27	−28:41:43.6	33.555	1.549	0.688	1.715	173	NO
CM40	G0.2474365 + 0.0095251	17:46:10.28	−28:43:11.8	33.555	1.863	0.662	1.773	167	NO
CM41	G0.2584992 + 0.0288511	17:46:07.34	−28:42:01.6	8.692	1.147	0.658	0.697	166	NO
CM42	G0.2576803 + 0.0252290	17:46:08.07	−28:42:10.9	16.980	6.136	0.647	6.469	163	YES
CM43	G0.2453628 + 0.0097262	17:46:09.94	−28:43:17.8	34.591	1.174	0.626	0.809	158	NO
CM44	G0.2454910 + 0.0010222	17:46:11.99	−28:43:33.7	83.283	4.220	0.611	4.026	154	YES
CM45	G0.2561685 + 0.0052779	17:46:12.52	−28:42:52.9	42.879	1.074	0.607	0.550	153	NO
CM46	G0.2412376 + 0.0067267	17:46:10.05	−28:43:36.1	25.267	1.583	0.594	1.150	150	NO
CM47	G0.2673045 + 0.0308945	17:46:08.11	−28:41:30.7	9.728	1.799	0.592	3.120	149	YES
CM48	G0.2718999 + 0.0255908	17:46:10.01	−28:41:26.5	−6.848	3.647	0.570	3.638	144	YES
CM49	G0.2540717 + 0.0241052	17:46:07.82	−28:42:24.1	24.231	4.852	0.556	4.864	140	NO
CM50	G0.2379498 + 0.0111649	17:46:08.55	−28:43:37.9	45.987	1.641	0.553	1.241	139	YES
CM51	G0.2564375 + 0.0208610	17:46:08.91	−28:42:22.9	7.656	3.531	0.545	2.843	137	NO
CM52	G0.2396789 + 0.0155356	17:46:07.77	−28:43:24.4	15.944	1.258	0.544	0.910	137	NO
CM53	G0.2672072 + 0.0262474	17:46:09.19	−28:41:39.7	11.800	2.678	0.529	5.735	133	YES
CM54	G0.2591622 + 0.0173474	17:46:10.12	−28:42:21.1	12.836	2.141	0.511	1.560	129	NO
CM55	G0.2668194 + 0.0286468	17:46:08.57	−28:41:36.4	13.872	4.400	0.490	3.069	124	NO
CM56	G0.2655322 + 0.0350864	17:46:06.88	−28:41:28.3	3.512	1.767	0.488	0.968	123	YES
CM57	G0.2391662 + 0.0109298	17:46:08.78	−28:43:34.6	52.203	3.941	0.469	2.405	118	YES
CM58	G0.2633546 + 0.0316127	17:46:07.38	−28:41:41.5	1.440	1.208	0.462	0.802	116	NO
CM59	G0.2565054 + 0.0213903	17:46:08.80	−28:42:21.7	11.800	2.355	0.450	1.856	113	NO
CM60	G0.2621404 + 0.0336065	17:46:06.75	−28:41:41.5	25.267	1.464	0.441	1.561	111	YES
CM61	G0.2523601 + 0.0128155	17:46:10.21	−28:42:50.5	12.836	3.974	0.409	2.917	103	YES
CM62	G0.2472548 + 0.0045354	17:46:11.42	−28:43:21.7	24.231	2.302	0.407	1.038	102	NO
CM63	G0.2536039 + 0.0149391	17:46:09.89	−28:42:42.7	12.836	3.988	0.405	4.935	102	YES

Table 5
(Continued)

ID	Candidate Name	R.A. (HH:MM:SS.s)	Decl. (DD:MM:SS.s)	Velocity (km s^{-1})	FWHM (km s^{-1})	I_{peak} (Jy beam^{-1})	Flux (Jy km s^{-1})	T_B K	Resolved?
CM64	G0.2490084 + 0.0117507	17:46:09.98	−28:43:02.8	18.016	3.543	0.398	4.842	100	YES
CM65	G0.2501440 + 0.0129301	17:46:09.87	−28:42:57.1	14.908	4.048	0.396	2.308	100	NO
CM66	G0.2586394 + 0.0164434	17:46:10.26	−28:42:24.4	15.944	3.890	0.391	2.884	98	YES
CM67	G0.2407096 + 0.0152850	17:46:07.98	−28:43:21.7	16.980	1.754	0.389	1.019	98	NO
CM68	G0.2501568 + 0.0109861	17:46:10.33	−28:43:00.7	24.231	2.672	0.369	1.039	93	NO
CM69	G0.2637776 + 0.0261113	17:46:08.73	−28:41:50.5	11.800	<1.036	0.366	0.329	92	NO
CM70	G0.2437590 + 0.0123602	17:46:09.10	−28:43:17.8	21.124	3.610	0.364	0.695	91	NO
CM71	G0.2537285 + 0.0112090	17:46:10.78	−28:42:49.3	22.159	1.804	0.362	0.833	91	NO
CM72	G0.2556194 + 0.0127505	17:46:10.69	−28:42:40.6	21.124	3.338	0.360	1.690	91	YES
CM73	G0.2439291 + 0.0125614	17:46:09.07	−28:43:16.9	25.267	2.348	0.359	1.394	90	NO
CM74	G0.2503013 + 0.0150752	17:46:09.39	−28:42:52.6	22.159	<1.036	0.346	0.257	87	NO
CM75	G0.2699078 + 0.0306250	17:46:08.55	−28:41:23.2	−7.884	5.485	0.341	15.765	86	YES
CM76	G0.2562854 + 0.0222324	17:46:08.57	−28:42:20.8	11.800	1.849	0.340	1.042	85	NO
CM77	G0.2510821 + 0.0115495	17:46:10.33	−28:42:56.8	27.339	2.811	0.337	1.618	85	NO
CM78	G0.2479022–0.0005347	17:46:12.70	−28:43:29.2	81.211	6.053	0.330	9.609	83	YES
CM79	G0.2527749 + 0.0127753	17:46:10.28	−28:42:49.3	16.980	3.675	0.312	2.886	78	YES
CM80	G0.2613076 + 0.0341730	17:46:06.49	−28:41:43.0	0.404	1.182	0.303	0.462	76	NO

weak masers near brighter sources, the central velocity of each maser candidate is indicated by a dashed line in each spectrum.

More than half of both the masers (37; 54%) and maser candidates (43; 54%) are spatially unresolved. These sources are deemed to be spatially resolved if their FWHMs are larger than twice the synthesized beam area. All of the masers and maser candidates also have relatively narrow line widths, with a mean FWHM for all cataloged sources of 3.6 km s^{-1}. More of the candidates (28; 35%) are spectrally unresolved than the masers (10; 15%), with sources deemed to be spectrally resolved if their FWHMs are larger than twice the channel resolution of 1.02 km s^{-1}. As we expect masers to have subthermal (<1 km s^{-1}) linewidths and generally to be spatially unresolved point sources, the large fraction of masers that are both spectrally and spatially resolved suggests that there is still confusion in this catalog, and that our observations are still underestimating the true number of maser sources in this cloud. Higher-resolution VLA observations should be able to confirm this and to determine the clumping properties of the CH_3OH masers in this cloud.

As the maser candidates appear, apart from their lower brightness temperatures, to be quantitatively similar to the masers (with similar fractions of both sources spatially and spectrally unresolved) we expect that the bulk of these sources will also prove to be masers. Possible exceptions to this are some of the candidate sources that have broader lines and more spatially extended emission. These sources (as well as regions of extended emission with $T_B \ll 100$ K that are not included in our catalogs) could represent thermal or "quasithermal" emission, as we discuss further below.

The number of CH_3OH sources detected in GCM0.253 +0.016 in our observations (148) is thus far unprecedented for a CMZ cloud. It is larger than the number of 36 GHz masers (10) recently identified by Sjouwerman et al. (2010) in the 50 and 20 km s^{-1} CMZ clouds, however this difference in the number of sources may be due in part to the fact that our observations are ∼5× more sensitive. It is also more than an order of magnitude greater than the number of 36 GHz sources (8) previously identified in this cloud by Yusef-Zadeh et al. (2013a). However, we should note that the positions for these sources given by Yusef-Zadeh et al. (2013a) do not match the positions of any of our masers, and it appears upon checking the archival data for these observations, that the previously published positions of 36 GHz sources in this cloud are incorrect. In the central part of the cloud, where we compare our data to the archival data from the Yusef-Zadeh et al. (2013a) observations, we detect three sources, at the positions of our brightest masers (M10, M18 and M25), but nothing at the published positions of three sources in this field (catalog numbers 42, 43, 44). We will assume that the number of sources cataloged by Yusef-Zadeh et al. (2013a) in this cloud can still be taken to be order-of-magnitude representative of what can be detected in this cloud at the sensitivity of their survey. Based on the yield of the Yusef-Zadeh et al. (2013a) study—356 individual 36 GHz sources over a surveyed area of 0.33 square degrees—our observations then suggest that clouds in the CMZ could host thousands of these masers, detectable by observing more clouds in the same way as for the GCM0.253 +0.016 data presented here, or potentially with a higher spectral-resolution survey than that conducted by Yusef-Zadeh et al. (2013a).

5.2. Distribution of Masers in GCM0.253+0.016

Focusing on the subset of sources that we can confirm to be masers, it can be seen from Figure 6 that these are distributed throughout the entire cloud. However, 44 of the masers (more then 60% of the total) are concentrated in the southern regions of the cloud, south of declination = −28°43′00.″0 (see Figure 6 left). These regions correspond to the regions denoted from the ammonia maps as the "C-arc" and the "bar" (see Section 4). Masers in the northern part of the cloud are typically more isolated than masers that fall in these other two regions. In addition to containing the majority of the maser emission, the southern region of the cloud also contains the brightest maser emission. With the exception of M3, all of the brightest masers are found in the southern region of the cloud. These brightest sources (M1 through M8) exhibit brightness temperatures in excess of 4000 K. In addition to the seven brightest masers, 25 additional masers have brightness temperatures in excess of 1000 K. The velocity range of the CH_3OH masers is from −5 to 50 km s^{-1}. Masers with velocities less than 20 km s^{-1} are seen

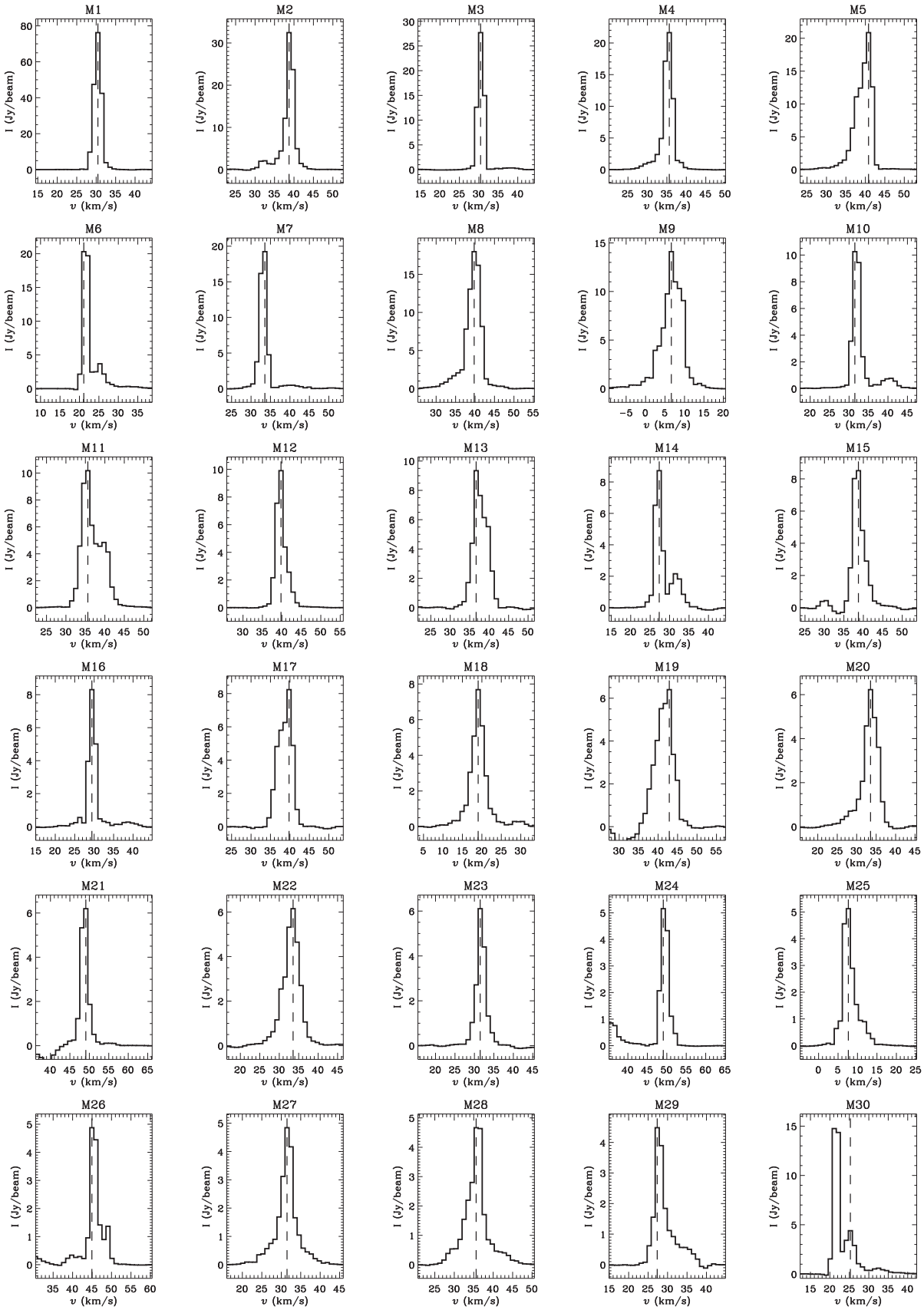

Figure 7. Spectra of all cataloged masers. Each spectrum corresponds to the pixel associated with the peak emission in the source defined by *Clumpfind*. The conversion factor to go from Jy to K is 250.5.

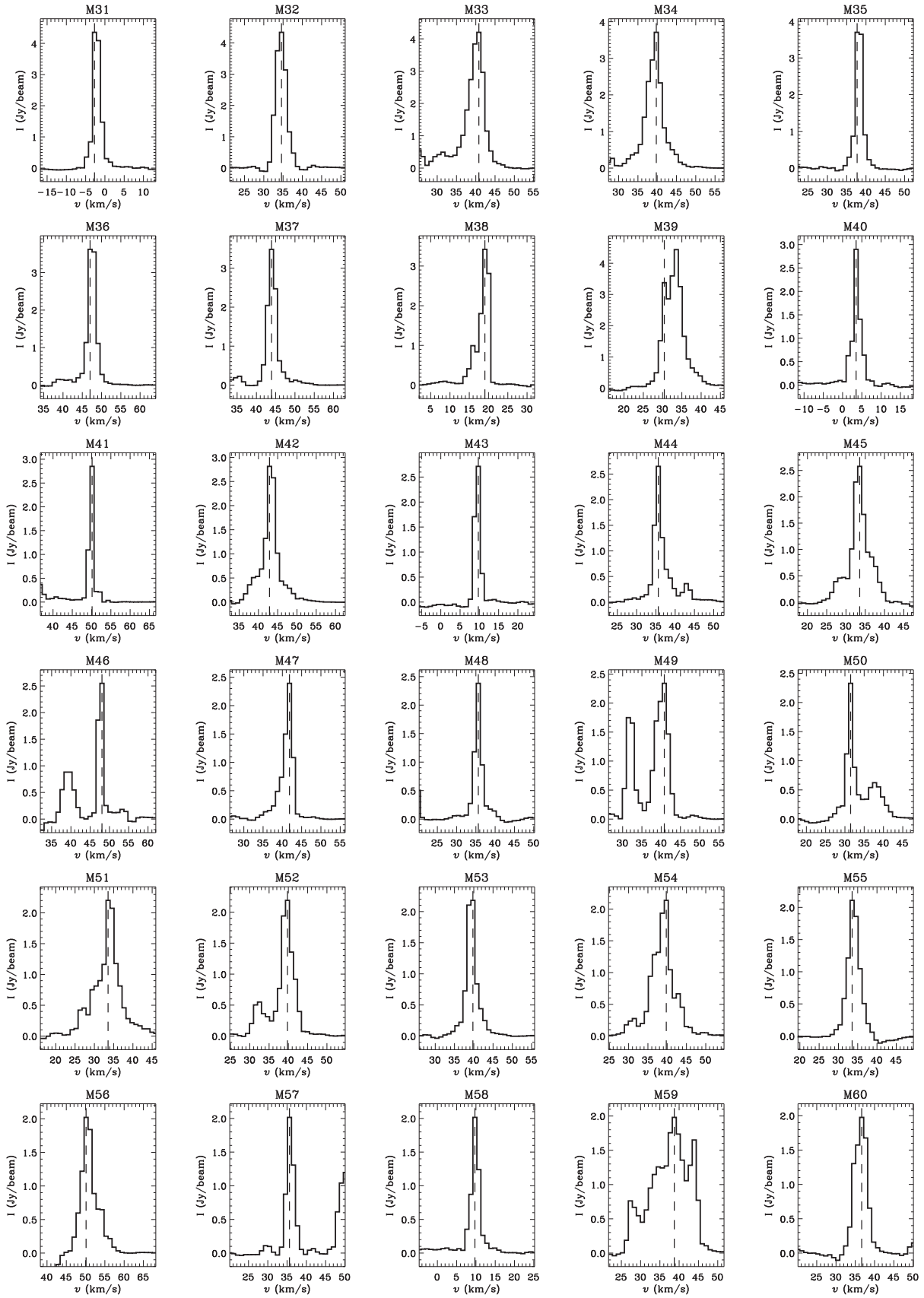

Figure 7. (Continued.)

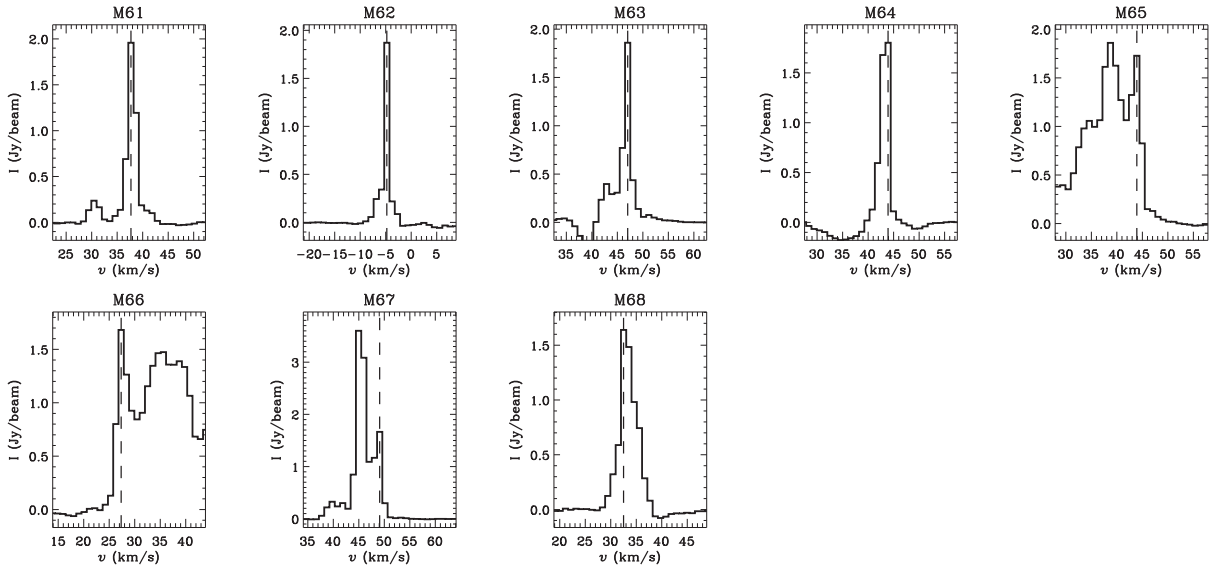

Figure 7. (Continued.)

only in the northern portion of the cloud, while masers at velocities greater than 20 km s^{-1} are seen throughout the cloud.

In general, the velocity distribution of the masers (−5 to 50 km s^{-1}) follows the same velocity distribution traced by NH_3 (3, 3) and seen in Figure 5. The northern part of the cloud shows maser emission occurring at roughly two velocities, ∼10 and 35 km s^{-1}, while the southern part of the cloud has a single, higher velocity component, ∼35 km s^{-1}. These maser velocities are similar to the NH_3 (3, 3) velocities, discussed in Section 4.2. The brightest masers, typically found in the southern part of the cloud, have velocities between 30 and 40 km s^{-1}, which is also the velocity of the brightest NH_3 (3, 3) emission.

The majority of the CH_3OH masers do not correspond to any continuum features, though a few exceptions are seen. The rising-spectrum continuum source C3 and the shell-like continuum source C9 are both associated with maser emission. The masers located in the vicinity of C3 (M10, M12, M32, M47, M49, M52, M53) are clustered around the continuum source, near a velocity of 40 km s^{-1}. We further discuss possibilities for the nature of this region, which is also associated with a peak in the millimeter dust continuum, in Section 6. The masers located in the vicinity of the shell source (M4, M20, M22, M14, M23), together with M6, M7, M27, M28, M30, and M33, form a nearly straight line at roughly constant declination across the cloud. This linear feature corresponds to the northeastern edge of the "bar" feature seen in NH_3 and discussed in Section 4. Two weaker masers (M44 and M54) are located near the top of the western edge of the shell.

The spatial distribution of the CH_3OH masers appears extremely similar to that of the dense gas traced by NH_3 (especially the NH_3 (3, 3) line) in GCM0.253+0.016. Like the morphology of the NH_3 lines in Figure 3 which are brightest in the southern part of the cloud, the majority of the brightest CH_3OH masers are also observed to be in the southern part of the cloud, and are associated with several bright, compact regions of NH_3. The CH_3OH masers also appear to be coincident with other prominent features traced in NH_3 (3, 3), such as the "C-arc" and, as previously mentioned, the "bar." A close correlation between CH_3OH and NH_3 emission, especially in the (3, 3) line of NH_3, has been previously noted for gas clouds in the GC (e.g., M–0.02–0.07, Sjouwerman et al. 2010). In other star-forming regions in the Galaxy, masers in the (3, 3) line of NH_3 have been observed to arise in the same region as collisionally excited CH_3OH masers (Mangum & Wootten 1994, e.g.,). While NH_3 (3, 3) masers have been suggested to exist in the CMZ cloud Sgr B2 (Martin-Pintado et al. 1999), in GCM0.253+0.016 all of the (3, 3) emission has brightness temperatures <100 K and so cannot be clearly attributed to masers. Finally, no CH_3OH emission is observed at the location of the H_2O maser identified by Lis et al. (1994).

In general, the maser candidates follow the same distribution as the masers: distributed throughout the cloud, with the majority lying in the southern half. There are also two CH_3OH maser candidates associated with the faint, 80 km s^{-1} component in the south-east portion of the cloud (CM44 and CM78). A number of the candidate sources (e.g., CM8, CM9, CM14, CM15, CM16, CM21, and CM28) also trace out a crescent-like feature the center of the cloud corresponding to the NH_3"C-arc." The typical brightness temperatures of these sources are 200–300 K, and they tend to have somewhat broader than normal measured FWHMs: ∼4.5–5 km s^{-1}. In addition to this main peak, the properties of which are cataloged, many of these spectra also exhibit a weaker superposed component having brightness temperatures of 40–80 K, and linewidths of 6–10 km s^{-1}, which appears as a plateau or "wings" in the spectra of many of these candidates (e.g., CM16). This weak and apparently spatially extended CH_3OH emission appears to be primarily associated with an analogous "c"-shaped feature in the 3 mm ALMA dust continuum map of Rathborne et al. (2014b). The low brightness temperature of the extended emission and its close correspondence with the 3 mm continuum could indicate that this region contains "quasithermal" emission from gas sufficiently dense that the maser in this line is quenched, analogous to that seen in the 44 GHz line in Sgr B2 (Mehringer & Menten 1997). If emission in this region is quasithermal in nature, then it is likely to be seen as a maser in other CH_3OH

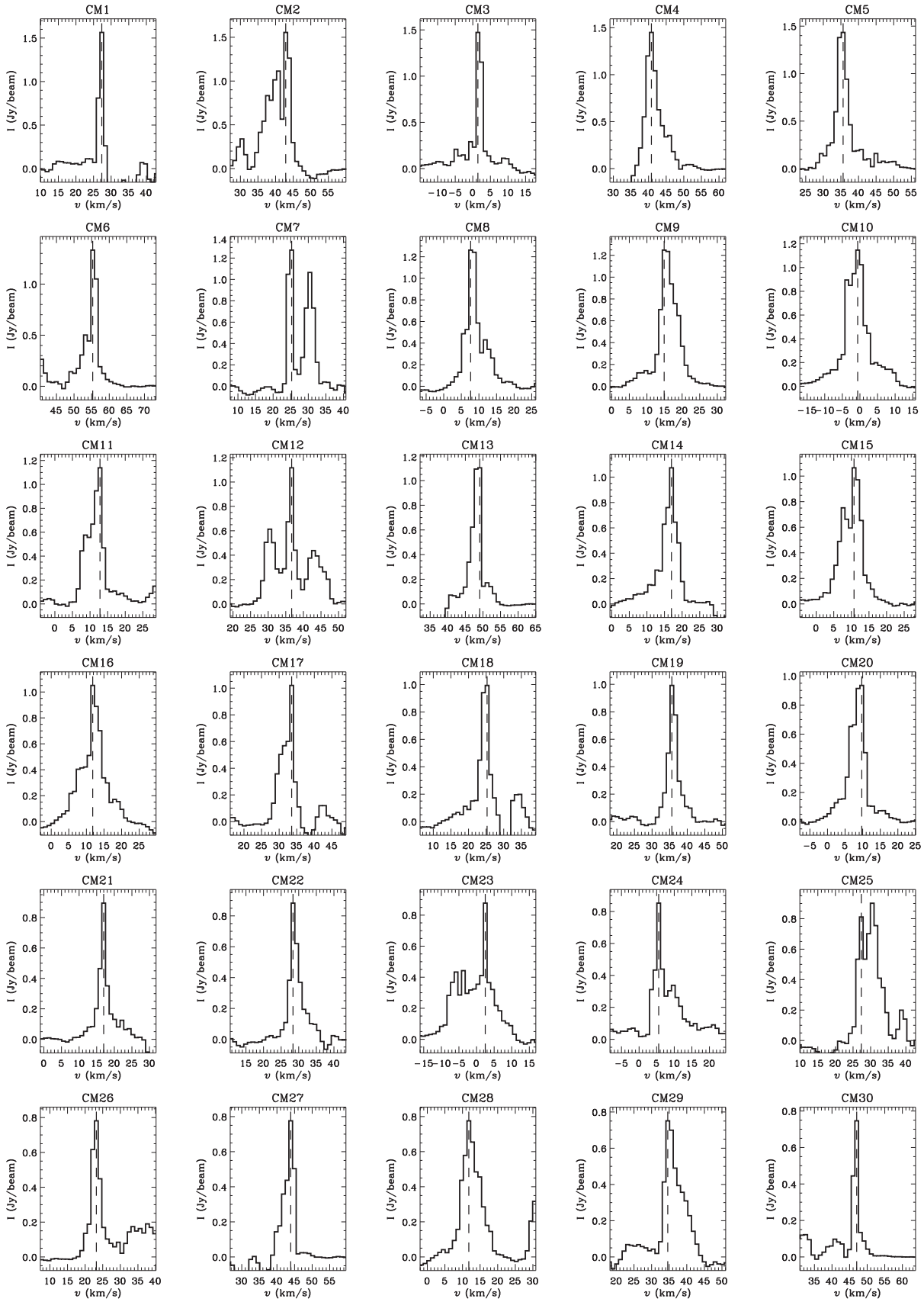

Figure 8. Spectra of all cataloged candidate masers. Each spectrum corresponds to the pixel associated with the peak emission in the source defined by *Clumpfind*. The conversion factor to go from Jy to K is 250.5.

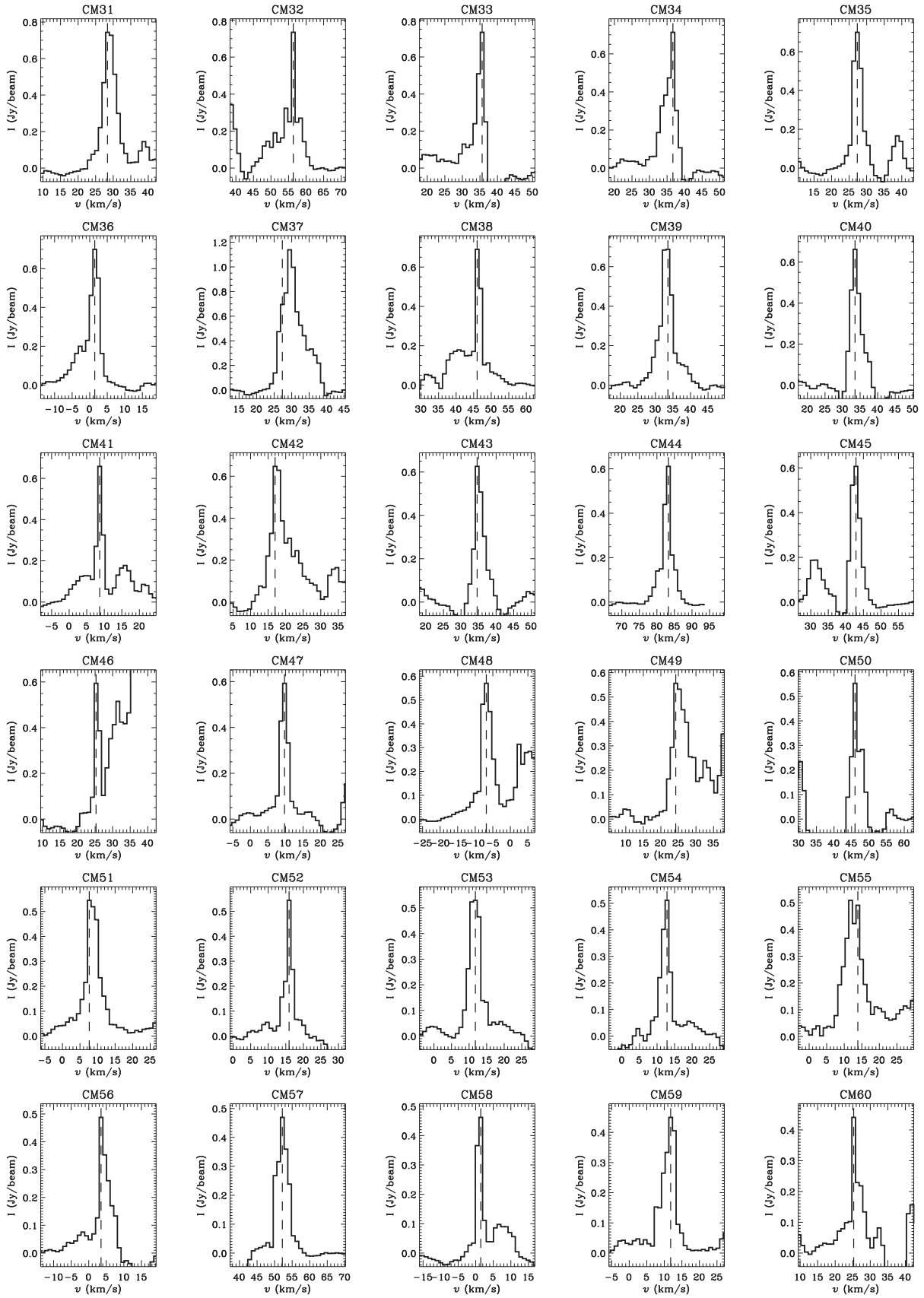

Figure 8. (Continued.)

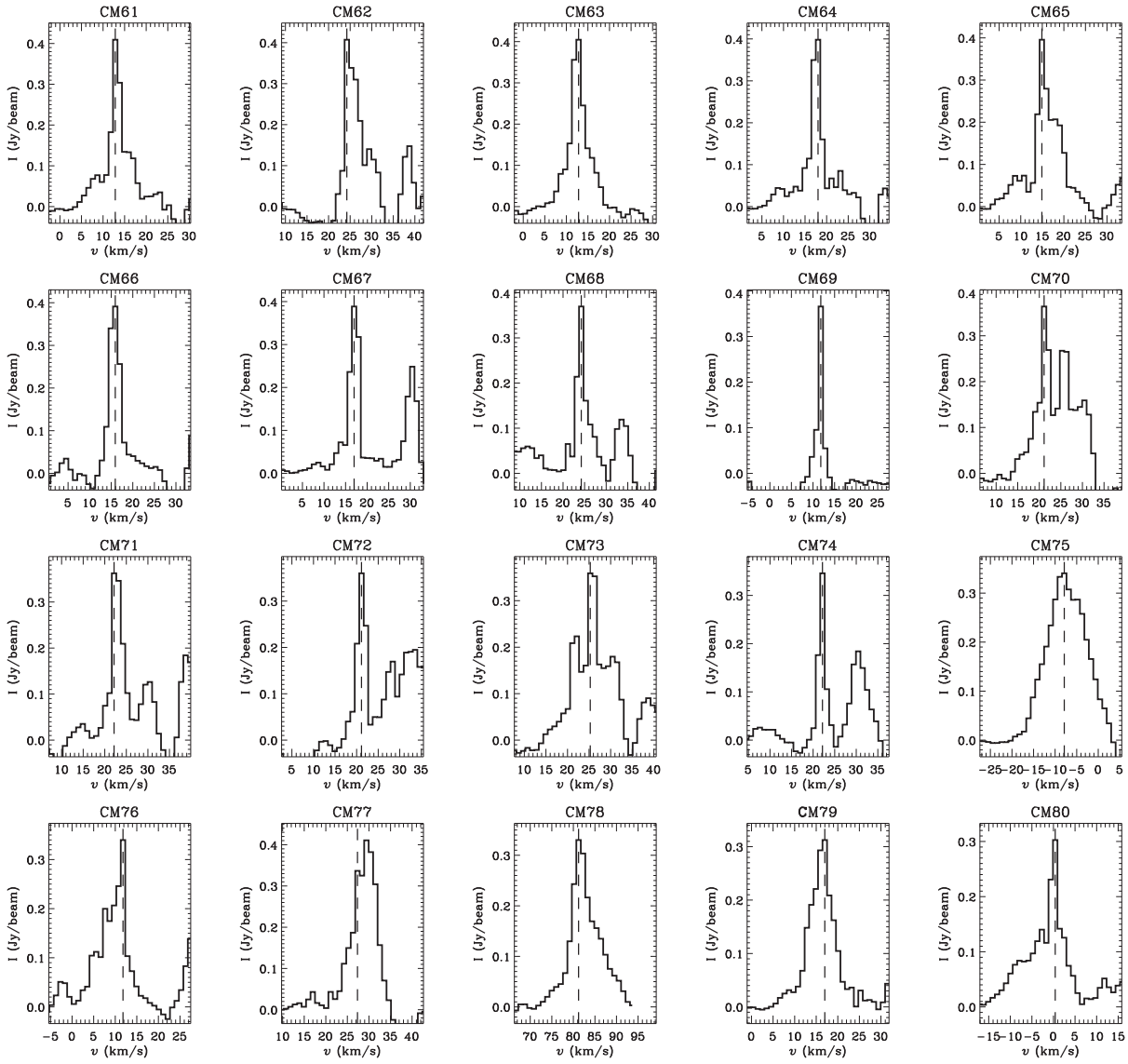

Figure 8. (Continued.)

transitions which quench at higher densities (e.g., 44, 84, or 96 GHz; Cragg et al. 1992; McEwen et al. 2014).

6. IS THERE ONGOING STAR FORMATION IN GCM0.253+0.016?

6.1. Origin of the CH_3OH Masers in GCM0.253+0.016

In the interstellar medium, CH_3OH and other "saturated" (hydrogen-rich) molecules are primarily believed to be formed on the surface of dust grains (Tielens & Hagen 1982; Charnley et al. 1992; Watanabe & Kouchi 2002), where CH_3OH and NH_3 are among the most abundant mantle species present relative to H_2O, as measured in both low and high-mass young stellar objects (YSOs) and cold cloud cores (Tielens & Allamandola 1987; Dartois et al. 1999; Pontoppidan et al. 2004; Gibb et al. 2004; Boogert et al. 2008; Öberg et al. 2011). Notably, for CH_3OH, the high abundances measured for maser sources are inconsistent with those predicted by gas-phase formation models (Menten et al. 1986; Hartquist et al. 1995). To get the CH_3OH off of the dust grains and into the gas phase in the observed large quantities then requires a mechanism to liberate the CH_3OH from the grain mantles. Proposed mechanisms include thermal desorption via heating from an embedded protostar, shocks, or cosmic rays (requiring grain temperatures $\gtrsim$90 K Tielens 1995; Brown & Bolina 2007), or nonthermal desorption processes including photodesorption via far-UV photons from cosmic ray interactions (Prasad & Tarafdar 1983; D'Hendecourt et al. 1985; Öberg et al. 2009a), grain sputtering, wherein the ice mantles of grains are dislodged via collisions (often in shocks) with other grains, neutrals, ions, or cosmic rays (Johnson et al. 1991; Caselli et al. 1997), and finally exothermic chemical reactions on the grain surfaces Duley & Williams (1993), Roberts et al. (2007). In particular, the presence of molecules formed on grains in relatively cool and dense environments requires an efficient nonthermal desorption process (Willacy & Williams 1993; Roberts et al. 2007; Öberg et al. 2009b; Caselli et al. 2012). In the CMZ, the abundance of 36 GHz CH_3OH sources has been suggested to be due to photodesorption from cosmic rays in this region Yusef-Zadeh

et al. (2013a). We reconsider this in the light of our new, high-resolution observations.

Our observations reveal that locations of CH_3OH emission are in general an excellent match to the 3 mm ALMA dust continuum map shown in Rathborne et al. (2014b). However, the observed CH_3OH masers are stronger and more numerous in the southern part of the cloud, while the stronger dust emission is found in the northern portion of the cloud, north of declination −28:42:34.2. If high column densities of CH_3OH simply originate from high column densities of dust, and if all of the excitation conditions are uniform, one might expect more masers in the northern parts of the cloud (we also note that no CH_3OH emission—thermal or maser—is detected toward the two strongest millimeter continuum peaks identified in Rathborne et al. 2014b). One possible explanation might be that, for much of the northern part of GCM0.253+0.016, the CH_3OH emission is quasithermal, and the masers are quenched in those regions which correspond to not just high column densities but high volume densities. With future observations, it should be possible to test this with observations of more highly excited masers (e.g., 44 GHz) which are quenched at higher densities (Cragg et al. 1992; Mehringer & Menten 1997; McEwen et al. 2014).

Another possibility is that the differences in the distribution and strengths of the masers are a result of variations in the geometry and kinematics of the cloud. Maser emission requires a velocity-coherent path length of gas for amplification of the emission. Class I CH_3OH masers are, for example, rarely seen in the high-velocity components of outflows, which is suggested to be because the longest gain paths are found perpendicular to the outflow, at velocities near the systemic values (Menten 1991, although as noted by Voronkov et al. 2014 this is also partially a selection effect). This makes it somewhat surprising to see a large quantity of masers in an extremely turbulent environment like that of GCM0.253+0.016. However, the vast majority of the detected masers are relatively weak (having intensities <5 Jy) which could be a result of the short coherent path lengths in this gas. The stronger masers observed in the southern parts of the cloud could be due to a geometrical effect, larger gain lengths can be had perpendicular to the motion of a shock front (Kaufman & Neufeld 1996), so if these masers trace a shock propagating in the plane of the sky, it could explain their enhanced intensity. However, are shocks really the mechanism responsible for generating these masers?

Prior observations would seem to be able to rule out thermal desorption processes for clouds in the CMZ like GCM0.253+0.016 which lack advanced stages of star formation. Measured dust temperatures in GCM0.253+0.016 are <30 K (Molinari et al. 2011; Longmore et al. 2012). Dust heating via cosmic rays should be relatively uniform (though it may be more efficient toward the edges of the cloud), and is further not predicted by models to yield dust temperatures above >40 K in GCM0.253+0.016 (Clark et al. 2013), so thermal desorption via cosmic ray heating can be ruled out. Heating via shocks or embedded sources might lead to discrete regions of higher dust temperatures, however the dust temperature maps of Longmore et al. (2012) show no signs of temperature variation that might indicate unresolved regions of higher temperatures. Although there is one location, C3, where the observed CH_3OH masers cluster around a bright radio continuum source, the masers generally do not correlate with the radio continuum, making the heating of dust from embedded sources an unlikely source for the liberated CH_3OH more globally observed in the widespread masers in this cloud. In general, the distribution and relatively low intensities of the continuum emission do not suggest that there are embedded, ionizing sources within this cloud (see below).

Among the previously listed nonthermal desorption processes, those most likely to be important in the unique environment of dense clouds in the CMZ are then sputtering from shocks and UV photodesorption due to cosmic rays. There is evidence in the CMZ for enhanced rates of both of these processes: both a cosmic ray ionization rate several orders of magnitude greater than the local value in the solar neighborhood ($\zeta_{GC} = 10^{-15}$–10^{-13} s^{-1}; Dalgarno 2006; Goto et al. 2013; Yusef-Zadeh et al. 2013b, 2013c; Harada et al. 2014, but see also van der Tak et al. 2006 who find $\zeta_{GC} \sim 10^{-16}$ s^{-1} in Sgr B2) and strong, widespread shocks (e.g., Martin-Pintado et al. 1997; Martín-Pintado et al. 2001; Rodríguez-Fernández et al. 2004; Mills & Morris 2013, although see also Yusef-Zadeh et al. 2013b, who suggest that a high SiO abundance in CMZ clouds could also be a consequence of a high cosmic ray ionization rate).

For CH_3OH to form via sputtering from shocks requires shocks of velocities sufficient to disrupt grain mantles; as species like CH_3OH are relatively loosely bound to these mantles, velocities $\gtrsim$10 km s^{-1} in continuous or C-type shocks are suggested to be sufficient to enhance the observed CH_3OH (and NH_3) abundances, while shock velocities >15 km s^{-1} will completely release the ice mantles into the gas phase (Caselli et al. 1997). For NH_3 and CH_3OH abundances to both be enhanced is consistent with our observations showing the morphologies of CH_3OH and NH_3 to be extremely similar on the scales probed here. Further, SMA observations by Johnston et al. (2014) illustrate the similar morphologies of CH_3OH and SiO, which suggests that the shocks may be yet stronger (shock velocities of 25–40 km s^{-1} are suggested for CMZ clouds from the abundances of complex molecules and models for their heating Martín-Pintado et al. 2001; Rodríguez-Fernández et al. 2004).

The question for GCM0.253+0.016 then becomes identifying the origin of these shocks. We suggest that shocks due entirely to protostellar outflows are unlikely, given the observed lack of 6 GHz radiatively excited (Class II) CH_3OH masers in this cloud (Caswell 1996; Caswell et al. 2010), which are typically found to be associated with regions of ongoing massive star formation (Voronkov et al. 2010). Elsewhere in the Galaxy, Class I masers are observed to be clustered around Class II masers (Slysh et al. 1994; Val'tts et al. 2000; Ellingsen 2005; Voronkov et al. 2014); the lack of Class II masers in GCM0.253+0.016 suggests that a different mechanism is responsible for the large CH_3OH abundances implied by the Class I masers here. In lieu of protostellar outflows, cloud–cloud collisions have been posited to enhance CH_3OH abundances in other CMZ clouds leading to Class I CH_3OH masers observed in Sgr A and Sgr B2 (Mehringer & Menten 1997; Sjouwerman et al. 2010). A cloud collision model has been independently suggested for GCM0.253+0.016 by Higuchi et al. (2014). However, more recent analyses favor a collapse model for the observed kinematics and morphology of the cloud instead (Rathborne et al. 2014a, 2015; J. M. D. Kruijssen et al. 2015, in preparation). Another possibility that should be investigated

for this cloud is an interaction with a supernova remnant: the GCM0.253+0.016 cloud overlaps in projection with a suggested supernova remnant identified by Kassim & Frail (1996). However, it has not yet been demonstrated that this supernova remnant is indeed located at the Galactic center.

An alternative to a model of shock-enhanced CH_3OH abundances in the CMZ is a high cosmic ray ionization rate. In brief: cosmic rays impact the dense gas, exciting the Lyman and Werner bands of H_2, generating a weak far-UV field in the cloud interior (Prasad & Tarafdar 1983). The UV photons are absorbed by molecules in the mantle exterior, which undergo photochemistry (photodissociation, diffusion and recombination), with some of the reaction products with excess energy being desorbed. Yusef-Zadeh et al. (2013a) favor this mechanism over cloud–cloud shocks for the generation of CH_3OH, as they assert that the effects of such shocks are limited to the cloud surfaces, although they do not consider the effects of smaller-scale turbulent shocks in cloud interiors. Given that the distribution of CH_3OH masers we observe is clustered and predominantly located in the southern part of the cloud, this might suggest that the masers are indeed limited to locations of large-scale and possibly even surface shocks, rather than more uniformly distributed in the cloud interior (though, as noted above, the apparently nonuniform distribution of CH_3OH masers could be an effect of density and/or orientation, and surface shocks could also result in a distribution of masers that, in projection, appears roughly uniform over the entire cloud).

Ultimately, both UV photodesorption from cosmic rays and grain mantle sputtering via shocks appear to be viable mechanisms for generating the observed CH_3OH abundances in GCM0.253+0.016. While our observations of stronger and more numerous masers in the southern part of GCM0.253+0.016 might slightly favor shocks as the primary mechanism for the abundant CH_3OH required to generate these masers, uncertainties as to the role gas density plays in quenching the 36 GHz maser in this cloud make it currently impossible to definitively determine the mechanism responsible. Various future observations could help to distinguish between shocks and cosmic rays as a mechanism for generating the observed CH_3OH abundances in the CMZ. First, as previously mentioned, observing other class I CH_3OH masers in CMZ clouds (e.g., the 44, 85, and 96 GHz masers) would aid in determining whether all class I maser transitions are stronger and more abundant in the southern part of GCM0.253+0.016, or if varying density in the cloud selectively quenches the 36 GHz masers. As these are the first observations of extremely abundant 36 GHz maser emission in a giant molecular cloud, it would also be valuable to search for similar emission outside of the CMZ, to determine whether this is truly a phenomenon unique to the inner few hundred parsecs of the Galaxy. While molecular clouds interacting with supernova remnants are not ideal targets as they could be expected to experience both enhanced shocks and cosmic ray ionization, other turbulent clouds lacking star formation should be searched on large-scales for class I CH_3OH maser emission. Finally, identifying the heating source for the molecular gas in the CMZ will likely also shed some light on the mechanism responsible for generating the observed abundances of CH_3OH and other molecules which are the product of grain-surface chemistry. As both cosmic rays and shocks are suggested to be the most likely source of cloud heating in the CMZ (e.g., Ao et al. 2013), it may be that the mechanism responsible for the heating drives not only the excitation of molecules in this region, but their chemistry as well.

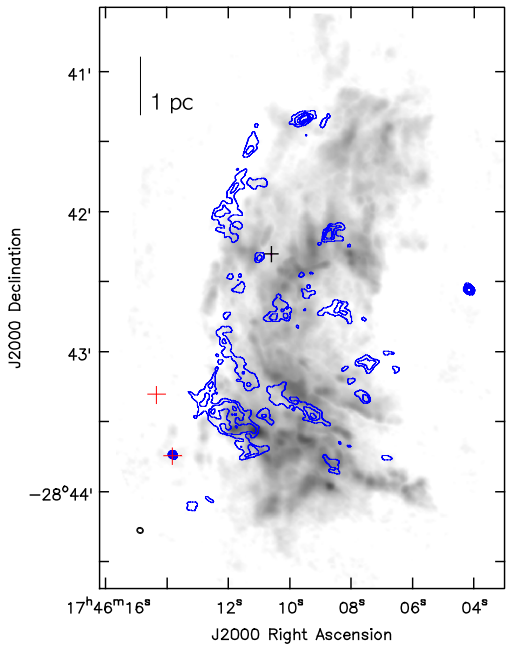

Figure 9. Comparison of the K-band continuum (contours) and the molecular gas, traced by NH_3 (3, 3). The black cross indicates the location of the H_2O maser from Lis et al. (1994), while the red crosses are candidate YSOs from An et al. (2011).

6.2. Nature of the Continuum Emission

6.2.1. The Ionization Source of the Extended Emission

Much of the continuum emission in GCM0.253+0.016 (e.g., regions C2, C7, and C9) is extended on scales of tens of arc seconds (1–2 pc at the Galactic center), forming rough arcs and filaments. We have argued, based on its roughly flat spectral index in several representative regions and its morphological similarity to the continuum emission seen at 90 GHz, that this emission is likely thermal, due to free–free radiation. Assuming this to be the case, the ionization source of this radiation needs to be determined.

Comparing the spatial distribution of the radio continuum to that of the molecular gas traced by the NH_3 (3, 3) line in Figure 9, it is clear that the continuum emission is primarily outlining the eastern edge of the cloud. The spatially extended regions C2, C7, and C9 all lie to the east of the peak of the molecular gas emission, roughly paralleling structures seen in the NH_3 line. In particular, C2 exactly parallels a similarly linear NH_3 feature 5″ to the west, while the regions C4, C7, and C8 all seem to trace the outer extent of the "C-arc" feature identified in NH_3 maps, with a similar spatial offset between the continuum and molecular line emission. C1 may also be a more northern extension of the same structure seen in C2. All together, this structure suggests that the extended emission in GCM0.253+0.016 is primarily at the cloud's surface, and that its ionization source is external to the cloud and to the east, perhaps a nearby O or B star. There is a known O4-6 supergiant located ∼11 pc away in projection to the east of the cloud, at R.A. = $17^h46^m28^s.2$, decl. = −28°39′20″ (Mauerhan et al. 2010). Its bolometric luminosity is estimated

to be 10^6 $L_\odot$. Using the parameters of Martins et al. (2005), a supergiant with this luminosity would have a Lyman continuum flux of log $Q_0 \sim 49.8$. The sum of the Lyman continuum fluxes for the regions in GCM0.253+0.016 that are cataloged in Table 3 is log $Q_0 \sim 47.8$. Assuming that the cloud intercepts a fraction of the Lyman continuum photons from this sources proportional to its surface area over the distance to the source squared, and that the surface area of GCM0.253+0.016 as seen by this source is the same as we see in projection (20.5 pc^2) then for the cloud to intercept ~1% of the Lyman continuum photons, the ionizing source would have to be at a distance of ~13 pc, which is consistent with its projected distance, making this a plausible source for ionizing the exterior of GCM0.253+0.016.

While the filament in C2 appears to have a parallel molecular counterpart, there do not appear to be any molecular counterparts to the linear continuum filament seen in the south of the cloud, next to the shell-shaped C9. This filament is also seen in the 90 GHz maps of Rathborne et al. (2014b). It is then not clear whether this is also an externally ionized surface feature. A comparison of the continuum emission to the enigmatic HCO^+ absorption filaments of Bally et al. (2014) does not show any correspondence: none of the HCO^+ filaments have a counterpart in either radio continuum or NH_3 emission. Neither do any of the continuum filaments appear to be oriented parallel to nearby HCO^+ filaments. Only the compact continuum source C4 appears to lie along the broad-line absorption filaments, near the junction of filaments 1 and 2, and could be just a chance superposition. However, the NH_3 emission just to the west of the bottom of the "C-arc" (at R.A. = $17^h46^m08^s$, decl. = −28°43′30″) does have a steep drop in its brightness, tracing a sharp, nearly linear edge. This edge corresponds to the "NLA 3" cluster of narrow-line HCO^+ absorption features identified by Bally et al. (2014), and it is possible that this edge could represent an analogous absorption feature. However, without the addition of single-dish data to provide a reliable flux zeropoint, it is not clear whether this edge seen in the NH_3 emission is actually an absorption feature, or simply the absence of emission.

6.2.2. Evidence for Ongoing Star Formation

The compact emission sources in and around GCM0.253+0.016 are of interest for potentially being signatures of the early stages of star formation in this cloud, either ultra- or hypercompact H II regions. Such regions would be expected to be optically thick, and to have slightly rising spectral indices. Of all of the sources we examine in Section 3.3, three (C3, C4, and C6) appear to have a rising spectrum. Of these, the radio peak of C3 is well aligned with the 90 GHz (Rathborne et al. 2014b) and 230/280 GHz (Kauffmann et al. 2013; Johnston et al. 2014) peaks, while the peak of C4 is slightly spatially offset (~3–5″) from two adjacent dust continuum peaks detected at 90 and 230 GHz. The stronger of these two peaks corresponds to the location of a previously identified water maser (Lis et al. 1994, marked with a black cross in Figure 9). Arguments against these radio sources being related to star formation in GCM0.253+0.016 are that (1) both C3 and C4 (and the more extended C6) are resolved out and not detected in the VLA B-configuration observations of Rodríguez & Zapata (2013), suggesting they are not intrinsically compact, and (2) the dust cores associated with C3 and C6 do not show expected signatures of self-gravitation in the column density PDFs of the dust emission constructed by Johnston et al. (2014) and Rathborne et al. (2014b). Of course, if the millimeter emission from these sources were instead from optically thick free–free emission instead of thermal dust emission, then any dust column densities inferred for these sources would not be valid. All three sources are assuredly thermal in nature, but whether we are seeing optically thick free–free emission or free–free emission mixed with dust (or a superposition of the two) cannot be determined using available data. Unfortunately, given the weakness of the continuum emission, we do not detect radio recombination line emission, so this cannot be used to determine the contribution of free–free radiation to these fluxes, or to assess whether it is likely to be optically thick. Ultimately, more sensitive observations at both higher and lower radio frequencies are needed to reconstruct the spectral energy distribution of these sources, and to determine their composition.

The other moderately strong continuum source we detect inside of the cloud, C1, has a flat spectrum consistent with optically thin free–free emission from other nearby, more extended regions of radio continuum emission that appear to trace the external ionization of the cloud, and it is not detected at 230 GHz by Johnston et al. (2014). The two compact continuum sources C5 and C10 are located outside of the bulk of dust and molecular gas in GCM0.253+0.016, and both have negative spectral indices that suggest their emission is primarily nonthermal. This would make it seem unlikely that they would be associated with star formation in this cloud. However, we do find that one of these sources, C10, is classified as a potential YSO by An et al. (2011) based on its infrared spectrum. Although it lies outside of the bulk of GCM0.253+0.016, it is spatially coincident with the 80 km s^{-1} cloud. However, without kinematic information from either our continuum observations or the infrared spectrum, it cannot be definitively associated with that cloud. A second YSO candidate identified by An et al. (2011) also lies near the 80 km s^{-1} cloud, however we do not detect a radio counterpart for this source. At present, there is thus no clear evidence from radio continuum observations for advanced stages of star formation in GCM0.253+0.016.

The other potential signature of early stages of star formation in GCM0.253+0.016, before the formation of compact H II regions, are the collisionally excited 36 GHz CH_3OH masers. Although the global CH_3OH emission in GCM0.253+0.016 is not likely due to star formation, some of the CH_3OH sources are clustered around the continuum sources C5 and C9. However, there are no CH_3OH masers near the water maser (and only weak ammonia emission associated with this source). At present, although such correlations are intriguing, there is no way to distinguish masers that could be associated with early stages of star formation and those endemic to the turbulent or cosmic-ray irradiated nature of the cloud.

7. CONCLUSIONS

We have detected new weak (<1 mJy) but widespread continuum emission from GCM0.253+0.016, much of which appears to be due to the external ionization of this cloud by an unknown source. The morphology of the continuum emission includes arcs, filaments, a shell, and multiple compact knots. We have also detected emission from eight transitions of NH_3, two transitions of HC_3N, and abundant emission from the 36.2 GHz collisionally excited maser line of CH_3OH. In total

we detect 68 sources whose nonthermal brightness temperatures prove them to be masers, and 81 candidate maser sources, which we expect higher-resolution followup observations will show to be masers as well. Although this is the largest number of these masers ever to be detected in a single molecular cloud, observations of widespread emission in this line throughout the central 200 parsec suggest that this may be a common feature of Galactic center clouds. As a source of relatively strong and ubiquitous emission, this maser (and potentially other collisionally excited CH_3OH masers), could in the future be a useful tracer of internal cloud kinematics in other turbulent environments, even other Galactic centers.

However, despite these new detections of continuum emission and numerous collisionally excited CH_3OH masers, we find no conclusive evidence for additional star formation in this cloud, apart from the signatures seen by others in a single dust core containing a water maser. We find that several recently identified compact thermal sources in this cloud which have been suggested to represent embedded star formation actually lie outside of the molecular gas emission, and appear to be mainly associated with more extended structures which we attribute to the external ionization of the cloud. This suggests that GCM0.253+0.016 truly is unique in the Galactic center, if not the entire Galaxy, as the only massive ($\sim 10^5\ M_\odot$) compact cloud not currently displaying advanced signatures of star formation (Ginsburg et al. 2012; Tackenberg et al. 2012; Urquhart et al. 2014).

Although observations of radio continuum can rule out the more advanced stages of star formation, in the complicated environment of the Galactic center it is not clear what would represent a "smoking gun" for early stages of star formation in a cloud. Signatures that are a reliable signpost of the onset of star formation elsewhere in the galaxy: collisionally excited 36 GHz masers tracing protostellar outflows, hot core chemistry, or elevated temperatures appear to simply be the norm in these clouds (e.g., Requena-Torres et al. 2006; Ao et al. 2013; Yusef-Zadeh et al. 2013a). Although it may be possible to identify kinematic features such as outflows in a region with simpler kinematics, the extreme turbulent motions of these clouds as a whole make it difficult to ascribe single features to the effects of just one forming star. So, while it appears unlikely that GCM0.253+0.016 hosts advanced star formation, earlier stages of star formation may still be hidden within.

We thank Jill Rathborne and Katharine Johnston for sharing their millimeter continuum data and for useful discussions. We also thank Steve Longmore, Diederik Kruijssen, Adam Ginsburg, and the anonymous referee for helpful comments which improved the final version of this paper. We additionally wish to thank the staff of the Karl G. Jansky Very Large Array, and especially to thank Dr. Claire Chandler for assistance with these observations. C.C.L., N.B., and E.A.C.M. acknowledge support from the NRAO Resident Shared Risk Observing (RSRO) program. E.A.C.M. also acknowledges support from the NRAO Student Observing Support program. C.C.L., N.B. and D.A.L. acknowledge that this material is based upon work supported by the National Science Foundation under grant No. AST-0907934.

REFERENCES

An, D., Ramírez, S. V., Sellgren, K., et al. 2011, ApJ, 736, 133
Ao, Y., Henkel, C., Menten, K. M., et al. 2013, A&A, 550, A135
Bally, J., Stark, A. A., Wilson, R. W., & Henkel, C. 1987, ApJS, 65, 13
Bally, J., Rathborne, J. M., Longmore, S. N., et al. 2014, ApJ, 795, 28
Boogert, A. C. A., Pontoppidan, K. M., Knez, C., et al. 2008, ApJ, 678, 985
Brown, W. A., & Bolina, A. S. 2007, MNRAS, 374, 1006
Caselli, P., Hartquist, T. W., & Havnes, O. 1997, A&A, 322, 296
Caselli, P., Keto, E., Bergin, E. A., et al. 2012, ApJL, 759, L37
Caswell, J. L. 1996, MNRAS, 283, 606
Caswell, J. L., Fuller, G. A., Green, J. A., et al. 2010, MNRAS, 404, 1029
Charnley, S. B., Tielens, A. G. G. M., & Millar, T. J. 1992, ApJL, 399, L71
Chen, X., Ellingsen, S. P., & Shen, Z.-Q. 2009, MNRAS, 396, 1603
Cheung, A. C., Rank, D. M., Townes, C. H., Thornton, D. D., & Welch, W. J. 1969, Natur, 221, 626
Clark, P. C., Glover, S. C. O., Ragan, S. E., Shetty, R., & Klessen, R. S. 2013, ApJL, 768, L34
Cragg, D. M., Johns, K. P., Godfrey, P. D., & Brown, R. D. 1992, MNRAS, 259, 203
Dahmen, G., Huttemeister, S., Wilson, T. L., & Mauersberger, R. 1998, A&A, 331, 959
Dalgarno, A. 2006, PNAS, 103, 12269
Dartois, E., Schutte, W., Geballe, T. R., et al. 1999, A&A, 342, L32
de Pree, C. G., Goss, W. M., & Gaume, R. A. 1998, ApJ, 500, 847
D'Hendecourt, L. B., Allamandola, L. J., & Greenberg, J. M. 1985, A&A, 152, 130
Duley, W. W., & Williams, D. A. 1993, MNRAS, 260, 37
Ellingsen, S. P. 2005, MNRAS, 359, 1498
Gaume, R. A., & Claussen, M. J. 1990, ApJ, 351, 538
Ghez, A. M., Salim, S., Weinberg, N. N., et al. 2008, ApJ, 689, 1044
Gibb, E. L., Whittet, D. C. B., Boogert, A. C. A., & Tielens, A. G. G. M. 2004, ApJS, 151, 35
Gillessen, S., Eisenhauer, F., Trippe, S., et al. 2009, ApJ, 692, 1075
Ginsburg, A., Bressert, E., Bally, J., & Battersby, C. 2012, ApJL, 758, L29
Goto, M., Indriolo, N., Geballe, T. R., & Usuda, T. 2013, JPCA, 117, 9919
Guesten, R., & Downes, D. 1983, A&A, 117, 343
Harada, N., Riquelme, D., Viti, S., et al. 2014, in IAU Symp. 303, ed. L. O. Sjouwerman, C. C. Lang, & J. Ott (Dordrecht: Kluwer), 139
Hartquist, T. W., Menten, K. M., Lepp, S., & Dalgarno, A. 1995, MNRAS, 272, 184
Higuchi, A. E., Chibueze, J. O., Habe, A., Takahira, K., & Takano, S. 2014, AJ, 147, 141
Ho, P. T. P., Jackson, J. M., Barrett, A. H., & Armstrong, J. T. 1985, ApJ, 288, 575
Hüttemeister, S., Wilson, T. L., Bania, T. M., & Martin-Pintado, J. 1993, A&A, 280, 255
Immer, K., Menten, K. M., Schuller, F., & Lis, D. C. 2012, A&A, 548, A120
Johnson, R. E., Donn, B., Pirronello, V., & Sundqvist, B. 1991, ApJL, 379, L75
Johnston, K. G., Beuther, H., Linz, H., et al. 2014, A&A, 568, A56
Jones, D. I. 2014, ApJL, 792, L14
Kalenskii, S. V., Johansson, L. E. B., Bergman, P., et al. 2010, MNRAS, 405, 613
Kassim, N. E., & Frail, D. A. 1996, MNRAS, 283, L51
Kauffmann, J., Pillai, T., & Zhang, Q. 2013, ApJL, 765, L35
Kaufman, M. J., & Neufeld, D. A. 1996, ApJ, 456, 250
Kruijssen, J. M. D., Dale, J. E., & Longmore, S. N. 2015, MNRAS, 447, 1059
Kruijssen, J. M. D., & Longmore, S. N. 2014, MNRAS, 439, 3239
Kruijssen, J. M. D., Longmore, S. N., Elmegreen, B. G., et al. 2014, MNRAS, 440, 3370
Kurtz, S., Hofner, P., & Álvarez, C. V. 2004, ApJS, 155, 149
Lada, C. J., Forbrich, J., Lombardi, M., & Alves, J. F. 2012, ApJ, 745, 190
Lis, D. C., & Menten, K. M. 1998, ApJ, 507, 794
Lis, D. C., Menten, K. M., Serabyn, E., & Zylka, R. 1994, ApJ, 423, L39
Longmore, S. N., Rathborne, J., Bastian, N., et al. 2012, ApJ, 746, 117
Longmore, S. N., Kruijssen, J. M. D., Bally, J., et al. 2013, MNRAS, 433, L15
Longmore, S. N., Bally, J., Testi, L., et al. 2013, MNRAS, 429, 987
Maddalena, R. J., & Thaddeus, P. 1985, ApJ, 294, 231
Mangum, J. G., & Wootten, A. 1994, ApJL, 428, L33
Martin-Pintado, J., de Vicente, P., Fuente, A., & Planesas, P. 1997, ApJL, 482, L45
Martin-Pintado, J., Gaume, R. A., Rodríguez-Fernández, N., de Vicente, P., & Wilson, T. L. 1999, ApJ, 519, 667
Martín-Pintado, J., Rizzo, J. R., de Vicente, P., Rodríguez-Fernández, N. J., & Fuente, A. 2001, ApJL, 548, L65
Martins, F., Schaerer, D., & Hillier, D. J. 2005, A&A, 436, 1049
Mauerhan, J. C., Muno, M. P., Morris, M. R., Stolovy, S. R., & Cotera, A. 2010, ApJ, 710, 706

Mauersberger, R., Henkel, C., Wilson, T. L., & Walmsley, C. M. 1986, A&A, 162, 199
McEwen, B. C., Pihlström, Y. M., & Sjouwerman, L. O. 2014, ApJ, 793, 133
Megeath, S. T., Allgaier, E., Young, E., et al. 2009, AJ, 137, 4072
Mehringer, D. M., & Menten, K. M. 1997, ApJ, 474, 346
Menten, K. 1991, in ASPC 16, Atoms, Ions and Molecules: New Results in Spectral Line Astrophysics, ed. A. D. Haschick, & P. T. P. Ho (San Francisco, CA: ASP), 119
Menten, K. M., Walmsley, C. M., Henkel, C., & Wilson, T. L. 1986, A&A, 157, 318
Mezger, P. G., & Henderson, A. P. 1967, ApJ, 147, 471
Mills, E. A. C., & Morris, M. R. 2013, ApJ, 772, 105
Molinari, S., Bally, J., Noriega-Crespo, A., et al. 2011, ApJL, 735, L33
Morimoto, M., Kanzawa, T., & Ohishi, M. 1985, ApJL, 288, L11
Morris, M. 1989, in IAUS 136, The Center of the Galaxy, ed. M. Morris (Dordrecht: Kluwer), 171
Morris, M. 1993, ApJ, 408, 496
Nakanishi, H., & Sofue, Y. 2006, PASJ, 58, 847
Öberg, K. I., Boogert, A. C. A., Pontoppidan, K. M., et al. 2011, ApJ, 740, 109
Öberg, K. I., Linnartz, H., Visser, R., & van Dishoeck, E. F. 2009a, ApJ, 693, 1209
Öberg, K. I., van Dishoeck, E. F., & Linnartz, H. 2009b, A&A, 496, 281
Panagia, N. 1973, AJ, 78, 929
Pihlström, Y. M., Sjouwerman, L. O., Frail, D. A., et al. 2014, AJ, 147, 73
Pillai, T., Kauffmann, J., Tan, J. C., et al. 2015, ApJ, 799, 74
Pontoppidan, K. M., van Dishoeck, E. F., & Dartois, E. 2004, A&A, 426, 925
Prasad, S. S., & Tarafdar, S. P. 1983, ApJ, 267, 603
Rathborne, J. M., Longmore, S. N., Jackson, J. M., et al. 2014a, ApJ, 786, 140
Rathborne, J. M., Longmore, S. N., Jackson, J. M., et al. 2014b, ApJL, 795, L25
Rathborne, J. M., Longmore, S. N., Jackson, J. M., et al. 2015, ApJ, 802, 125
Reid, M. J., Menten, K. M., Brunthaler, A., et al. 2014, ApJ, 783, 130
Requena-Torres, M. A., Martin-Pintado, J., Rodríguez-Franco, A., et al. 2006, A&A, 455, 971
Roberts, J. F., Rawlings, J. M. C., Viti, S., & Williams, D. A. 2007, MNRAS, 382, 733
Rodríguez, L. F., & Zapata, L. A. 2013, ApJL, 767, L13
Rodríguez-Fernández, N. J., Martín-Pintado, J., Fuente, A., & Wilson, T. L. 2004, A&A, 427, 217
Sjouwerman, L. O., Pihlström, Y. M., & Fish, V. L. 2010, ApJL, 710, L111
Slysh, V. I., Kalenskii, S. V., Valtts, I. E., & Otrupcek, R. 1994, MNRAS, 268, 464
Tackenberg, J., Beuther, H., Henning, T., et al. 2012, A&A, 540, A113
Tielens, A. G. G. M. 1995, in ASPC 73, From Gas to Stars to Dust, ed. M. R. Haas, J. A. Davidson, & E. F. Erickson, 3
Tielens, A. G. G. M., & Allamandola, L. J. 1987, in NATO ASIC Proc. 210, Physical Processes in Interstellar Clouds, ed. G. E. Morfill, & M. Scholer (Dordrecht: Reidel), 333
Tielens, A. G. G. M., & Hagen, W. 1982, A&A, 114, 245
Urquhart, J. S., Moore, T. J. T., Csengeri, T., et al. 2014, MNRAS, 443, 1555
Val'tts, I. E., Ellingsen, S. P., Slysh, V. I., et al. 2000, MNRAS, 317, 315
van der Tak, F. F. S., Belloche, A., Schilke, P., et al. 2006, A&A, 454, L99
Vogel, S. N., Genzel, R., & Palmer, P. 1987, ApJ, 316, 243
Voronkov, M. A., Caswell, J. L., Ellingsen, S. P., et al. 2012, in IAU Symp. 287, ed. R. S. Booth, W. H. T. Vlemmings, & E. M. L. Humphreys (Dordrecht: Kluwer), 433
Voronkov, M. A., Caswell, J. L., Ellingsen, S. P., Green, J. A., & Breen, S. L. 2014, MNRAS, 439, 2584
Voronkov, M. A., Caswell, J. L., Ellingsen, S. P., & Sobolev, A. M. 2010, MNRAS, 405, 2471
Watanabe, N., & Kouchi, A. 2002, ApJL, 571, L173
Willacy, K., & Williams, D. A. 1993, MNRAS, 260, 635
Williams, J. P., de Geus, E. J., & Blitz, L. 1994, ApJ, 428, 693
Yanagida, T., Sakai, T., Hirota, T., et al. 2014, ApJL, 794, L10
Yusef-Zadeh, F., Cotton, W., Viti, S., Wardle, M., & Royster, M. 2013a, ApJL, 764, L19
Yusef-Zadeh, F., Wardle, M., Lis, D., et al. 2013b, JPCA, 117, 9404
Yusef-Zadeh, F., Hewitt, J. W., Wardle, M., et al. 2013c, ApJ, 762, 33
Zylka, R., Guesten, R., Henkel, C., & Batrla, W. 1992, A&AS, 96, 525